Tectonophysics 926 (2026) 231114

Contents lists available at ScienceDirect

Tectonophysics

journal homepage: www.elsevier.com/locate/tecto

P-wave seismic interferometric profile within the Granada Basin (Southern-Spain)

C. Araque-Pérez [a,*], D. Stich [a,b], T. Teixido [a], E. Carmona [a], J. Morales [a,b], F. Mancilla [a,b]

[a] Instituto Andaluz de Geofísica y Prevención de Desastres Sísmicos, Universidad de Granada, C. Prof. Dr. Clavera, 12, Granada 18011, Andalusia, Spain
[b] Departamento de Física Teórica y del Cosmos, Facultad de Ciencias, Universidad de Granada, Av. Fuente Nueva, Granada 18071, Andalusia, Spain

ARTICLE INFO

Keywords:
Seismic interferometry
P-wave imaging
Microseismicity
Granada basin

ABSTRACT

A detailed seismic imaging profile of the subsurface beneath the Granada Basin (southern Spain) has been generated using P-wave seismic interferometry applied to local microseismicity. The analysis, conducted along a 44 km long, SW–NE trending transect, used 117 well-located earthquakes (12–17 km depth) recorded by only three local stations between 1984 and 2024. Our imaging methodology applies Common Interferometry Points (CIPs), a geometric construction that approximates the stationary phase points for impulsive seismic sources. CIPs provide a robust spatial organization of the interferometric traces, enabling improved stacking, enhanced reflector continuity, and extensive subsurface illumination despite the sparse station coverage. The resulting seismic section reveals the complex crustal architecture in the central part of the basin, including a mid-crustal reflector at 10–15 km depth. This low-angle structure is interpreted as being part of the basal detachment of the basin, decoupling the brittle upper crust from the ductile part. The detachment roots major normal faults that generate *horst*-and-*graben* structures within the basin. Integration with four decades of instrumental seismicity supports this structural interpretation and demonstrates the potential of the method to recover deep crustal structure in tectonically active and logistically challenging regions.

1. Introduction

The Granada Basin (GB), located in southern Spain within the Betic Cordillera, is a Neogene intramontane basin that represents a key area for understanding the tectonic evolution of the western Mediterranean region (Fig. 1A) (Rodríguez-Fernández et al., 1984; Morales et al., 1990; Galindo-Zaldívar et al., 1993; Booth-Rea et al., 2007; Azañón et al., 2013). This basin lies at the boundary between the Internal and External Betic domains, forming a geologically complex zone where dense fault networks have developed under varying stress conditions in the context of plate convergence between Eurasian and North African as well as regional extensional processes (Sanz de Galdeano et al., 2003; Meijninger, 2006; Benito et al., 2010). At present, it is considered the most seismically active region of the Iberian Peninsula (Reicherter et al., 2003; Carmona et al., 2009; Lozano et al., 2022; Madarieta-Txurruka et al., 2022).

A notable feature of the basin architecture is the hypothesized presence of a brittle basal detachment (BD) at depths of 10–15 km (Morales et al., 1997; Madarieta-Txurruka et al., 2021; Lozano et al., 2022; Stich et al., 2024), inferred from seismicity patterns and supported by other geophysical data (Galindo-Zaldívar et al., 1996; Martin-Rojas et al., 2023). However, its precise geometry remains poorly constrained due to the lack of detailed imaging. While previous studies suggested links between shallow fault systems and this deeper detachment (Galindo-Zaldívar et al., 1996; Madarieta-Txurruka et al., 2021; Araque-Pérez et al., 2025), these proposed connections have not been validated by direct imaging so far.

Seismic interferometry is a useful geophysical technique used to extract subsurface information by correlating seismic wavefields recorded at different receivers (Claerbout, 1968). In the context of natural earthquakes, interferometry enables the retrieval of empirical Green's functions between receiver pairs by exploiting earthquake-generated signals, without the need for controlled seismic sources (Wapenaar et al., 2008; Curtis et al., 2009; Curtis and Halliday, 2010; Wapenaar et al., 2010; Galetti and Curtis, 2012). This makes it a cost-effective tool for imaging geological structures, supporting earthquake hazard assessment, lithospheric studies, and exploration geophysics.

To better constrain the geometry of the deep structure, the main objective of this study is to assess the feasibility of applying seismic interferometry to earthquake waveform data in order to construct a deep

---

* Corresponding author.
E-mail address: carlos.araque@ugr.es (C. Araque-Pérez).

https://doi.org/10.1016/j.tecto.2026.231114
Received 27 October 2025; Received in revised form 30 January 2026; Accepted 2 February 2026

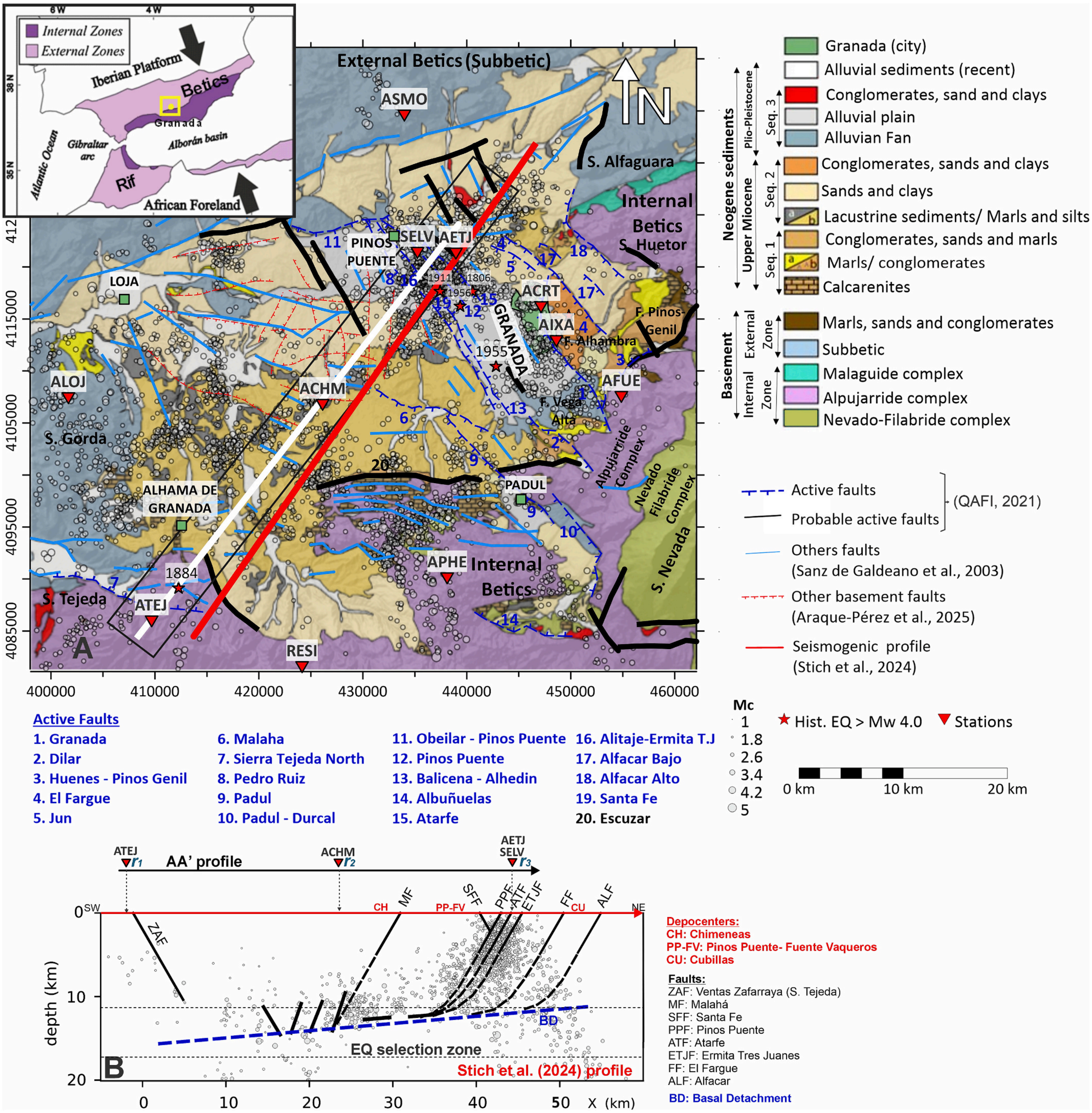

Fig. 1. (A) Geological, structural, and seismicity map of the Granada Basin, compiled from Sanz de Galdeano et al. (2003), the Quaternary Active Fault Information Catalogue (QAFI, 2021), Araque-Pérez et al. (2025), and Stich et al. (2024). The inset map shows the regional tectonic framework of the Betic Cordillera, including the Internal and External Betic domains, and the yellow rectangle indicates the location of the Granada Basin shown in panel A. The white line marks the AA' profile selected for the seismic interferometric experiment and shows the locations of the seismic stations along the profile: ATEJ (Sierra Tejeda), ACHM (Chimeneas), SELV (Sierra Elvira), and AETJ (Ermita de los Tres Juanes). Owing to their close spatial proximity (distance <2 km), the northern stations SELV and AETJ were treated as a single effective station (see Table 1). The black rectangle delineates the surface projection of the Fresnel zone calculated for a representative depth of 17 km. (B) Seismogenic profile from Stich et al. (2024), corresponding to the red line shown in panel A, included here as a reference framework for the seismogenic characterization of the region. Earthquake hypocentres are plotted by moment magnitude (Mw), consistent with panel A. The "EQ selection zone" denotes the area used for event selection, defined by the intersection of the Fresnel zone and the target depth range. This profile provides an independent control point for the interpretation of the seismic interferometry section later presented in this study. (For interpretation of the references to colour in this figure legend, the reader is referred to the web version of this article.)

structural model of the GB. To this end, we analyze four decades of earthquake data (1984–2024) from the Andalusian Geophysical Institute (IAG-UGR) by applying P-wave interferometry and organizing the data using the Common Interferometry Point (CIP), a geometric framework proposed and developed in this study. The CIP is introduced as a practical organizational construct, conceptually inspired by Common Midpoint (CMP) and Common Depth Point (CDP) methods (Yilmaz, 2001), but adapted here for earthquake-based interferometry under irregular source–receiver geometries. It approximates the stationary-phase region for impulsive sources and facilitates the stacking of interferometric traces. This workflow involves applying inter-receiver interferometry, reorganizing the retrieved empirical Green's functions into CIP gathers, and performing travel-time corrections to produce a stacked seismic section along a longitudinal profile aligned with the seismic stations and earthquake hypocenters. Our goal is to provide new constraints on the geometry of the Granada Basin and to present a practical method for deep imaging in regions where traditional seismic surveys are hindered by urbanization, environmental restrictions, or logistical limitations.

2. Geological setting

2.1. General framework

The GB is a tectonic depression forming part of the Betic Cordillera (Fig. 1A). It is bounded to the southeast by the Sierra Nevada, the highest mountain range in the region, to the northeast by the Sierra de Huétor, and to the west by the Sierra Gorda. These mountain ranges serve as geographical barriers that influence both the extent and configuration of the basin. Tectonically, the basin is situated within one of the most seismically active zones of the Iberian Peninsula, rendering it the region with the highest seismic hazard (Gil-Zepeda et al., 2002; Lozano et al., 2022). However, the basin exhibits moderate seismicity when compared to other regions worldwide.

This basin is recognized as a Neogene pull-apart basin, which has been progressively infilled with sedimentary deposits from the Late Miocene to the Quaternary (Morales et al., 1990; García-Alix et al., 2009; Pérez-Peña et al., 2015). It extends approximately 65 km east-west and 40 km north-south, covering a total area of ~2600 km^2 within the Betic Cordillera (Sanz de Galdeano and Cruz, 2016). Persistent subsidence in the central sector has facilitated the accumulation of sedimentary sequences that reach thicknesses of up to 2 km (Morales et al., 1990; Rodríguez-Fernández and Sanz de Galdeano, 2006). The oldest stratigraphic units within the basin correspond to deposits of Tortonian age, consisting mainly of conglomerates, calcareous sandstones, and marls, indicative of the early sedimentary evolution of the basin (Araque-Pérez et al., 2025).

The basin is situated on top of the boundary between the two main units of the Betic mountain range, the External and Internal Betics. The internal zone consists of three superimposed complexes: Nevado-Filábride, Alpujárride and Maláguide, primarily composed of metamorphic rocks (Meijninger, 2006; Benito et al., 2010; Sanz de Galdeano and Cruz, 2016). The External Zone is a fold-and-thrust belt primarily composed of Mesozoic-Cenozoic sedimentary rocks (including conglomerates, marls, and sandstones) from the Iberian Paleomargin. Both formations overlie Triassic units that constitute the Subbetic Complex (Balanya and Garcia-Dueñas, 1987; Monie et al., 1991; García-Dueñas et al., 1992; Sanz de Galdeano et al., 2001; Cruz et al., 2005; Azañón et al., 2013).

2.2. Seismo-tectonic context

Three different classes of geodynamic models have been traditionally invoked to explain the tectonic evolution of the Betic Cordillera and associated extensional processes. The first class of models suggests a classical subduction process (Araña, 1974; Wortel et al., 1992; Pedrera et al., 2011; Ruiz-Constán et al., 2011). A second class of models introduces the concept of lithospheric delamination (García-Dueñas et al., 1992; Calvert et al., 2000). The third class corresponds to slab rollback models (Wortel and Spakman, 2000; Rosenbaum et al., 2002; Booth-Rea et al., 2007; Chertova et al., 2014). Recent studies have provided further evidence and imaging to support the leading role of slab rollback processes, particularly highlighting segmentation along subduction boundaries due to slab rollback along Subduction-Transform Edge Propagator (STEP) faults (Duggen et al., 2003; Martínez-Martínez et al., 2006; Garcia-Castellanos and Villaseñor, 2011; Mancilla et al., 2013, 2015). These findings reinforce the slab rollback hypothesis as the most updated framework for interpreting the seismotectonic evolution of the GB.

The GB developed during the Late Miocene under a general intraplate strike-slip tectonic regime with a dominant extensional component-oriented WSW–ENE (Agosta et al., 2012). Its tectonic evolution has been governed by alternating phases of crustal compression and extension. Compressional episodes led to horizontal shortening and thickening of the crust, which contributed to regional uplift and structural deformation. In contrast, extensional phases promoted crustal thinning and subsidence, leading to the formation of *grabens* and the relative uplift of *horst* blocks (Galindo-Zaldívar et al., 1999; Gil-Zepeda et al., 2002). This Neogene extensional basin (Pérez-Peña et al., 2015) has progressively accumulated sedimentary deposits from the Late Miocene to the Quaternary (Rodríguez-Fernández and Sanz de Galdeano, 2006).

Local seismicity in the GB can be monitored since the installation of a local seismic network in the 1980s, operated by the Andalusian Institute of Geophysics at Granada University (IAG-UGR, for its acronym in Spanish). In this period earthquakes have not exceeded magnitude Mw 5.0 and show mostly shallow depths above 20 km, with a notable concentration of hypocenters between 10 and 15 km (Galindo-Zaldívar et al., 1999; Morales et al., 1997; Stich et al., 2003, 2020, 2024; Madarieta-Txurruka et al., 2021, 2022). Local microseismicity (Fig. 1A) is characterized by the occurrence of seismic swarms with spatially concentrated epicenters (Carmona, 2009; Carmona et al., 2009; Stich et al., 2024).

Seismicity is associated with NW–*SE*-trending high-angle normal faults that appear to merge into a low-angle fault beneath the basin (Fig. 1B). This observation suggests that extensional deformation is predominantly accommodated by motion along this deeper low-angle structure. The most recent notable seismic sequence occurred in the Santa Fe area between December 2020 and August 2021, reaching a maximum magnitude of Mw 4.5 (Lozano et al., 2022; Madarieta-Txurruka et al., 2022; Morales et al., 2025). During this period, over 3000 earthquakes were recorded, with most events occurring at depths between 2 and 5 km. Of these, 353 were reportedly felt by the local population (Luque-Espinar and Mateos, 2023).

2.3. Fault systems

The GB hosts active fault systems (Fig. 1A, blue lines), primarily high-angle normal faults trending in NW–SE and E-W orientations. Many of these structures have contributed to the formation of *horst* and *graben* structures (Sanz de Galdeano et al., 2012). Their geometry and vertical extent suggest reactivation during multiple tectonic phases, particularly the Tortonian and Pliocene (Pérez-Peña et al., 2015). Displacements along these faults created accommodation space in *graben* zones, enabling significant sediment accumulation, while *horst* blocks show limited sedimentation, indicating that basement structure has directly influenced facies distribution and sedimentary architecture (Viseras et al., 2003; Rodríguez-Fernández and Sanz de Galdeano, 2006).

At depth, the fault distribution appears linked to BD zones inferred at 10–15 km, though these have not been directly imaged (Morales et al., 1997; Madarieta-Txurruka et al., 2023; Stich et al., 2024). Their connection to mapped faults is mainly interpretative, supported by earthquake relocations and cluster analysis (Fig. 1B), which delineate seismogenic zones and hint at a structural link between surface and deep features (Araque-Pérez et al., 2025).

Among the mapped faults, particular emphasis is placed on those most relevant to the structural and seismotectonic analysis developed in this study. The Sierra Tejeda North Fault (#7), located in the southwestern basin near Ventas de Zafarraya fault (ZAF), is historically associated with the 1884 Andalusian earthquake (Mw 6.5–6.7), representing one of the most hazardous structures in the region despite the overall low background seismicity (Reicherter et al., 2003). The Malahá Fault (#6, MF), a southwest-dipping normal fault in the central basin with a NW-SE direction, located near the modeled seismogenic profile and plays a key role in the deformation field analyzed in this work (Sanz de Galdeano et al., 2003; Araque-Pérez et al., 2025). The Escúzar Fault (#20, ESZ), located in the central-southwestern margin of the basin with a W-E to WNW-ESE trending, is a normal fault characterized by a steep dip angle (~60°) and contributes to accommodating extensional deformation although it is considered as a possible active fault (Sanz de Galdeano et al., 2003).

Additionally, the fault cluster defining the Sierra Elvira *half-graben* includes the Pinos Puente, Alitaje, Atarfe, and Ermita de Tres Juanes faults. These are all high-angle normal faults trending NW–SE, central to crustal subsidence and extension in the central GB (Sanz de Galdeano et al., 2012; Sanz de Galdeano et al., 2003). Their seismic activity is supported by recent earthquake swarms, including the 2020–21 Santa Fe–Atarfe sequence (Mw up to 4.5), where hypocentral depths and focal mechanisms align with these faults (Lozano et al., 2022; Stich et al., 2024).

3. Seismic interferometry overview

The fundamental principle behind seismic interferometry is that wavefields recorded at two distinct locations contain information about the medium between them (Claerbout, 1968; Schuster, 2009; Curtis et al., 2006; Snieder et al., 2006). By cross-correlating these recordings, it is possible to approximate the waveforms that would be obtained if one of the locations acted as a virtual source and the other as a receiver. This methodology has been widely applied in seismic imaging, monitoring temporal variations in the crust, and characterizing seismotectonic processes (Shapiro and Campillo, 2004; Wapenaar et al., 2010). Several types of interferometric approaches exist, including inter-receiver, inter-source, and source–receiver interferometry (Wapenaar et al., 2008; Galetti and Curtis, 2012). Under the assumption of impulsive or sufficiently broadband sources and adequate spatial sampling, the empirical Green's function between two receivers can be approximated by cross-correlation of their recorded wavefields and summation over sources distributed in space (Claerbout, 1968; Wapenaar, 2004; Wapenaar and Fokkema, 2006):

$$G(x_A, x_B, t) \approx \int_S u(x_A, t)^* u(x_B, t)\, dS \tag{1}$$

where $u(x_A, t)$ and $u(x_B, t)$ are the recorded wavefields at receivers x_A and x_B, respectively, and * denotes cross-correlation. In practice, source-time-function and radiation-pattern effects are mitigated by stacking interferometric responses from multiple earthquakes with diverse locations and mechanisms, as implemented in this study.

One geometrical configuration of seismic interferometry is shown in Fig. 2, where two seismic signals $u_A(t)$ and $u_B(t+\tau)$, recorded at points A and B, are cross-correlated. The time lag τ represents the differential arrival time of wavefronts from an earthquake S_i at receivers r_A and r_B. The function $G(r_B, r_A; t)$ represents the Green's function in the time domain described previously by Eq. (1).

An alternative formulation approximating the reflective response between two stations is given by (Claerbout, 1968; Wapenaar, 2003):

$$R(x_B, x_A, t) + R(x_B, x_A, -t) \approx \delta\left(x_{H,B} - x_{H,A}\right)\delta(t)$$

$$-\sum_i T\left(x_B, x_S^{(i)}, t\right)^* T\left(x_A, x_S^{(i)}, -t\right) \tag{2}$$

Here, R denotes the reflection response between surface locations x_A and x_B, and T represents the upward transmission from subsurface sources $x_S^{(i)}$. The term $\delta(t)$ models an ideal impulsive source, which may be approximated using the autocorrelation of the source waveform.

Building upon this theoretical foundation, we developed a workflow to apply seismic interferometry using P-wave signals generated by earthquakes. The approach focuses on extracting, processing, and cross-correlating seismic phases recorded at different stations to reconstruct virtual receiver–receiver responses along the surface. In the following sections, we first introduce the concept of Common Interferometry Points (CIP), then discuss specific considerations for P-wave interferometry, and therefore describe the criteria for event selection, the data processing workflow, and the procedures used to construct a seismic image without active sources.

3.1. Common Interferometry Points (CIP)

The CIP is employed here as a practical geometric construction to organize interferometric data generated by impulsive sources, such as earthquakes, within a non-diffuse wavefield context. This approach

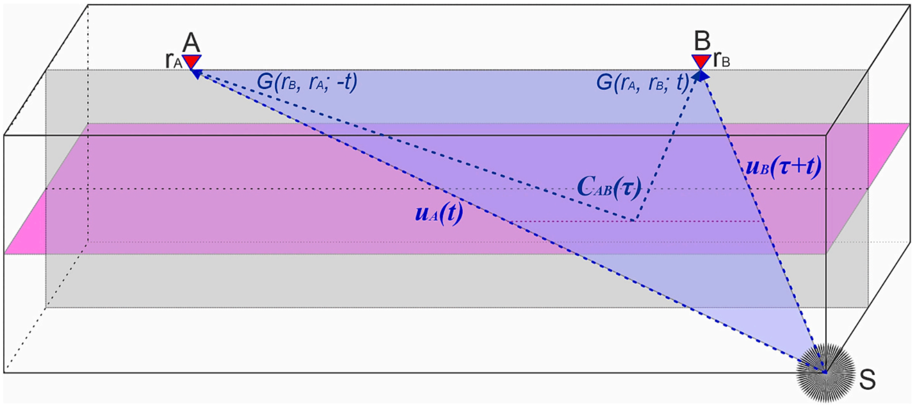

Fig. 2. General schematic of seismic interferometry, illustrating how recordings at two receivers can be used to retrieve a virtual-source response. The signals $u_A(t)$ and $u_B(t)$ represent the seismic wavefields recorded at receivers A and B from a source S. The function $C_{AB}(\tau)$ denotes the cross-correlation between the two recordings as a function of the time lag τ. The quantity $G(r_A, r_B, t)$ represents the retrieved empirical Green's function between the two receivers. (For interpretation of the references to colour in this figure legend, the reader is referred to the web version of this article.)

enables an increase in the number of effective subsurface illumination points when only a limited set of seismic stations is available but numerous natural seismic events occur between them. This framework is particularly valuable in earthquake-based interferometry, where the spatial distribution of natural sources is often irregular and asymmetrical relative to the recording array.

The CIP is defined through the following procedure: (1) for a given earthquake “source” (S_1) and receiver (r_1), the midpoint (M_1) along the direct ray path between them is computed at depth; (2) the equivalent midpoint (M_2) between the same source (S_1) and a second receiver (r_2) is also calculated along the corresponding ray path; and (3) the CIP is defined as the centroid of the triangle formed by the two midpoints and the source location (S_1) at depth (Fig. 3A–C).

This construction can be interpreted in a manner consistent with the stationary phase principle. The main contributions to the cross-correlation integral arise from points of constructive interference, which, for a virtual reflection between two receivers, correspond to subsurface locations that are simultaneously illuminated by both source–receiver ray paths. In the proposed geometry, these locations are constrained to lie within the region bounded by the triangle defined by the earthquake source S_1 and the midpoints M_1 and M_2. The centroid of this triangle therefore provides a stable geometric average for the most probable subsurface location of a virtual scatterer, ensuring that it lies within a physically meaningful region common to both correlated wave paths.

Conceptually, the CIP is analogous to a CDP (Common Depth Point) in that stacking at this location enhances the coherence of P—P reflections (Yilmaz, 2001). Geometrically, the CIP behaves more like a CDP rather than a CMP (Common Mid Point), as its position shifts toward the receiver closest to the earthquake when the source–receiver geometry is asymmetric (Fig. 3B–C). When the earthquake happens to be located exactly midway between two receivers, the CIP coincides with both the CMP and the CDP (Fig. 3A). This geometric definition recalls the Common Conversion Point (CCP) approach (Zhu and Kanamori, 2000), although in this study it is used solely as a practical tool to reorganize interferometric traces and to account for asymmetric source-receiver configuration. However, unlike CCP, no P—S conversion is assumed in the geometric definition of the CIP. Although P—S converted energy is generally present in earthquake recordings, the interferometric workflow focuses on the wavefield window between the direct P arrival and the S phase, where P—P energy is expected to dominate on the vertical component. This choice follows standard practice in earthquake-based seismic interferometry, where restricting the analysis to P-dominated windows improves coherence and reduces cross-term contamination from converted phases (e.g., Casas et al., 2020).

For example, in a simple configuration with two earthquakes and three receivers, the P-wave paths yield limited coverage (Fig. 3D). When the cross-correlated signals are organized using the CIP concept, these same data can produce multiple probable illumination points (six in this example; Fig. 3E), substantially increasing the spatial sampling of the subsurface without adding more stations or sources.

3.2. *Considerations on seismic interferometry for P-waves*

Seismic interferometry is most commonly applied using ambient noise due to its near-isotropic source distribution and multiple scattering, which comes close to the theoretical premises of the methodology, such as uniform wavefield illumination and efficient cancellation of source effects (Snieder and Hagerty, 2004; Shapiro and Campillo, 2004; Campillo and Paul, 2008; Vasconcelos and Snieder, 2008). In contrast, using P-waves from earthquakes imposes several limitations related to the nature of the source distributions and wavefield asymmetries.

- Source Distribution and Directivity: Earthquakes are typically unevenly distributed in space, leading to anisotropic illumination that can bias Green's function retrieval (Shearer, 2009). In earthquake-based interferometry, such effects are commonly mitigated by restricting the analysis to source–receiver configurations located within or near stationary-phase regions, where constructive interference dominates the correlation integral. This geometric selection strategy is explicitly adopted in the present study through the use of the CIP, which focuses on source–receiver pairs that maximize coherent P—P energy despite asymmetric illumination.

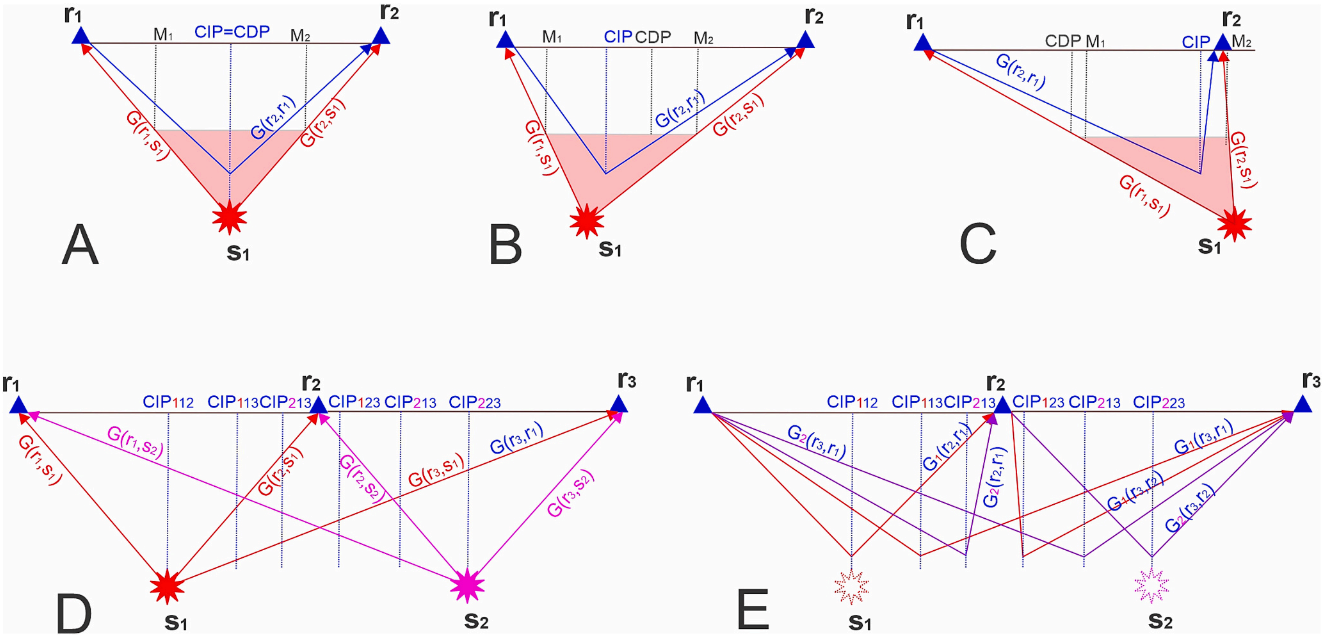

Fig. 3. Common Interferometry Point (CIP) configuration using two receivers (r_j, $j = 1,2,3$) and earthquakes (S_i, $i = 1,2$). (A) Symmetric case where the earthquake lies midway between the two receivers. (B) Earthquake located between the two receivers but asymmetrically. (C) Earthquake located outside the inter-receiver span. (D) Example with two earthquakes and three receivers. (E) Using the CIP concept within the context of P-wave seismic interferometry yields multiple probable illumination points (six in this example).

- Source Effects: Variations in focal mechanisms and the signature of finite source processes affect the phase and amplitude of P-waves, reducing waveform coherence (Ben-Zion, 2001). Preprocessing steps such as band-pass filtering and amplitude normalization help suppress these differences and enhance consistency (Bensen et al., 2007).
- Converted Phases: PS and PP conversions can introduce coherent noise into the P-wave window. Although PS waves are typically of lower amplitude, they can distort cross correlations. Band-pass filtering (5–20 Hz) and deconvolution with source autocorrelations can attenuate these effects and improve signal clarity (Curtis et al., 2006; Aki and Richards, 2002).
- Low Amplitudes and Noise: Direct P-waves may have lower amplitudes and be more susceptible to noise compared to coda or surface waves. Stacking multiple events enhances the signal-to-noise ratio and suppresses incoherent noise (Snieder and Hagerty, 2004).
- Receiver Geometry and Frequency Dependence: The effectiveness of P-wave interferometry depends on the receiver configuration and incident wavefield diversity. Dense azimuthal coverage improves the quality of reconstructed responses, whereas sparse or directional illumination can degrade coherence (Wapenaar et al., 2010).

4. Methodology

4.1. IAG-UGR local earthquake catalogue

The IAG-UGR earthquake catalogue was used for this study, encompassing the period from 1984 to 2024. Over these four decades, approximately 27,000 local earthquakes have been recorded by the local seismic stations (red triangles in Fig. 1A). A concise overview of the seismic stations comprising the IAG-UGR network, together with a summary of the network configuration and the velocity model employed for earthquake location, is presented in the Supplementary Material (Table SP1). The spatial distribution of seismicity at the GB becomes clear from double difference relocations for a subset of the IAG-UGR catalogue, including approximately 3000 events with magnitudes larger than 2 and RMS values below 0.3 (Stich et al., 2024). Relocated seismicity is shown in Fig. 1A, highlighting a primary concentration of shallow earthquakes (2–15 km depth) between the Cubillas (CU) and Pinos Puente–Fuente Vaqueros (PP–FV) depocenters. A second zone of heightened activity is located between the CU and Granada (GR) depocenters, characterized by slightly greater average depths. In the southern and south-western sectors, seismicity appears more diffuse, while discrete clusters are observed near the western station ALOJ. The main concentration of local microseismicity is observed near stations SELV and AETJ, where a high density of shallow events (mostly <10 km) indicates predominant near-surface tectonic activity. Deeper events, mainly concentrated in the depth interval from 10 to 15 km, can be observed over a wide area, forming a prominent mid-crustal seismicity layer that has been associated with the basal detachment beneath the basin (Galindo-Zaldívar et al., 1999; Morales et al., 1997, 2025; Stich et al., 2024; Madarieta-Txurruka et al., 2021). These spatial patterns of seismicity are important for interpreting the network's recording geometry and designing seismic interferometric analyses.

4.2. P-wave seismic interferometry procedure

4.2.1. Earthquake selection

As an initial step of the analysis, a representative 2D profile was selected to provide robust control over the structural interpretation. The selected transect (white line in Fig. 1A) traverses the basin in a SW–NE direction and is located near the seismogenic structure proposed by Stich et al. (2024) (red line in Fig. 1A). The profile is aligned with the approximate SW direction of basin extension (e.g., Mancilla et al., 2013; Martin-Rojas et al., 2023) and covers the most active seismic zones in the basin. The profile has seismic stations at the SW termination (Sierra Tejeda, ATEJ, r_1), in the central part (Chimeneas, ACHM, r_2) and at the NE termination (Sierra Elvira, SELV, r_3, and Ermita de los Tres Juanes, AETJ, r_3), ensuring broad coverage of CIPs. AETJ (operative since 2012) is the successor of SELV (operative since 1997), which had to be reinstalled due to a change of use at the original emplacement. For proper geometric illumination, only earthquakes with epicenters located within 2 km of the straight line connecting each station pair were selected. This threshold corresponds to the surface projection of the Fresnel zone calculated for a representative depth of 17 km, which defines an effective illumination corridor of approximately ±2 km around the station-to-station profile (black frame in Fig. 1A). In addition, the selected events were further restricted to hypocentral depths between 12 and 17 km, ensuring consistency between the source–receiver geometry and the target depth range of the interferometric analysis. This combined geometric and depth-based selection enhances waveform coherence and ensures consistent subsurface illumination.

Earthquake data were selected from the double-difference hypocenter catalogue of the IAG-UGR (Stich et al., 2024), which provides more robust locations and reduced depth uncertainties compared to the routine catalogue. Only events with magnitudes ≥ 2 were considered to ensure sufficient signal-to-noise ratio for interferometric processing. The selected events are predominantly concentrated within the depth range associated with the brittle–ductile transition of the basal detachment (BD; blue dashed line in Fig. 1B), which constitutes the one of the main targets of the present analysis. The resulting dataset comprises 142 earthquakes, with a maximum magnitude of 4.5. An additional selection criterion was waveform quality. Only events with clearly identifiable P- and S-wave arrivals and cross-correlation similarity coefficients above 0.6 between reciprocal signals recorded at station pairs were retained. As a result, 18% of the events recorded at stations r_1 and r_2, and 48% of those at station r_3, were rejected, keeping a final dataset of 117 earthquakes for interferometry (see selected earthquakes list in the Table SP3 within Supplementary Material). The stations SELV and its successor AETJ were treated as a single receiver (r_3), projected onto the AA′ cross-section. A summary of the selected events is presented in Table 1. The azimuthal distribution of selected events is not uniform, and our setup prioritizes subsurface illumination along the AA′ transect rather than isotropic wavefield sampling.

4.2.2. Signal processing

The data processing workflow (depicted in Supplementary Material, Figure SP1) for generating the seismic interferometry image section comprises:

Stage 1. The preprocessing of seismic records to ensure data consistency and enhance the quality for the subsequent interferometric analysis (Fig. 4A). Initially, the acquisition geometry was defined by three receiver stations (r_n, where $n = \{1,2,3\}$) and 117 local earthquakes (S_m) that fulfill the quality criteria. The spatial distribution of events—confined within the Fresnel illumination zone and aligned along the selected seismicity corridor—are delineated by the black frame in Fig. 1A and by the dashed lines in the profile presented in Fig. 1B (EQ selection zone), with the selected events shown in Fig. 5A.

Following a direct current (DC) offset correction, the continuous waveforms were resampled to a uniform rate of 100 Hz. For each selected earthquake, individual seismic traces corresponding to single-station recordings were extracted using fixed 60-s time windows centered on the P- and S-wave arrival times obtained from the earthquake catalogue, preserving absolute time stamps (Universal Time, UTC) for consistent temporal alignment across stations. To improve the signal-to-noise ratio, a bandpass filter between 0.5 and 20 Hz was applied, attenuating low-frequency drifts and high-frequency noise while enhancing the dominant energy band of body waves (Bensen et al., 2007; Wapenaar et al., 2010). Subsequently, the waveform segment between the P- and S-wave arrivals was isolated to retain the most coherent and impulsive portion of the signal for interferometric processing. Finally, each extracted trace was normalized by its

Table 1
Event data from stations.

Station	X (m)	Y (m)	Z (m.s.l)	RID	Offset (km)	Ev	EvU	QC (%)
ATEJ	409,681.33	4,085,923.04	1470	*r*1	0	142	117	82
ACHM	426,128.25	4,106,737.74	825	*r*2	26.5	142	117	82
SELV-AETJ	437,102.05	4,120,625.83	700	*r*3	44.2	42	22	52

X, Y, Z: UTM coordinates (WGS84, zone 30 N) in metres. Z indicates elevation above sea level.
RID: Receiver identification within the cross-section.
Offset: Distance between each receiver and the zero point of the profile, in kilometres.
Ev: Number of events recorded at each receiver. EvU: Number of events with a good signal-to-noise ratio used.
QC (%): Percentage of high-quality events recorded at each station.

maximum absolute amplitude, scaling the signal between −1 and 1. This normalization corresponds to a simple amplitude scaling and does not involve one-bit normalization or spectral whitening, which are commonly applied in ambient-noise interferometry (Bensen et al., 2007). While this procedure suppresses true amplitude information, it is appropriate for enhancing waveform coherence in earthquake-based interferometric cross-correlation analyses.

Stage 2. The second stage centered on extracting coherent seismic information from station pairs that recorded the same earthquake (Fig. 4B). For each event, the corresponding waveforms were grouped according to the involved receiver pairs (as shown Fig. 2) to process signals from a common source.

The interferometric analysis in Stage 2 is performed on waveform segments extracted between the P- and S-wave arrivals, resulting in an effective time window shorter than the original 60-s window used in Stage 1. Consequently, the autocorrelations are centered at the midpoint of the reduced window (17.5 s for the example shown in Fig. 4B). To characterize the individual propagation paths at each station, autocorrelations were computed, capturing the local impulse response of the medium. These autocorrelations were subsequently used in Stage 3 for deconvolution, helping to attenuate residual source and site effects in the cross-correlated signals.

Subsequently, cross-correlations were computed for each station pair to reconstruct the seismic response between them using eq. (1). This procedure effectively attenuates the influence of the earthquake source and produces virtual source wavefields, in accordance with interferometric theory (Schuster and Zhou, 2006; Torii et al., 2008). In total, 326 causal cross-correlations were computed, with each station pair providing the two reciprocal propagation paths.

Stage 3. The third stage concentrated on integrating the interferometric responses from Stage 2 into a geometry that enhances subsurface illumination. This was achieved by computing the CIPs for each receiver pair and associated earthquake (see Fig. 3 explanation and Fig. 5A blue points as the CIP calculated). This geometric construction ensures that the CIP lies within the region most likely to concentrate constructive interference between correlated wavefields, effectively acting as a spatial reference point for trace organization and stacking. Details of CIP fold and coverage are provided in the Supplementary Material (Figure SP2), where 161 CIPs are included from 117 earthquakes recorded by the ATEJ–ACHM station pair and 22 earthquakes recorded simultaneously by the three stations.

The cross-correlated signals obtained in Stage 2 were then convolved with a 5 Hz zero-phase Ricker wavelet (Ricker, 1953), as illustrated in Fig. 5B, in order to stabilize their spectral content and enhance the resolution of coherent arrivals. Following this, the convolved Ricker's traces were deconvolved using the stacked autocorrelations (Fig. 5B) computed in Stage 2. This step attenuated residual source and site effects, improving the clarity and symmetry of the recovered Green's functions without the need for explicit spectral whitening or water-level stabilization.

Once processed, the resulting interferometric traces were grouped into three virtual shot gathers, G_1, G_2, and G_3, each corresponding to one of the real stations acting as the virtual source origin. Within each gather, all individual empirical Green's functions are displayed prior to stacking and are sorted laterally according to the surface position of their associated CIP. A preliminary geometric time-reference shift was applied to each trace to account for differences in the distance between the virtual source and the corresponding CIP, referencing the data to the theoretical P-wave travel time from the virtual source to the CIP (Fig. 6), computed using the layered velocity model of Serrano (1999; see Table SP2 in the Supplementary Material). This operation establishes a common temporal reference within each virtual gather without modifying the relative lag of the interferometric correlations.

In addition, static corrections were introduced to account for near-surface velocity variations (Araque-Pérez et al., 2025; Table SP4 in Supplementary Material) and topography. Finally, the corrected traces were sorted by absolute offset relative to each virtual source, preparing the dataset for the imaging stage (Fig. 7 A-C) that could be treated analogously to conventional seismic reflection data.

Stage 4. The final stage of the workflow involved constructing the seismic image from the previously processed traces. The data were first organized into the CIP domain using a bin size of 75 m. Functionally comparable to Common Depth Point (CDP) domain in reflection seismology (Yilmaz, 2001), the CIP construction enables stacking based on the virtual reflection geometry associated with source configurations.

Subsequently, Normal Move-Out (NMO) corrections were applied. While static corrections addressed near-surface heterogeneity and elevation differences, NMO specifically compensated for travel-time variations associated with geometric effects due to varying offsets from virtual sources. These corrections used a composite velocity model derived from Serrano (1999), Serrano et al. (2024), and Araque-Pérez et al. (2025; see Tables SP4-SP5 in Supplementary Material) and were implemented individually for each virtual gather. This procedure aligns reflection events to a common zero-offset time (Fig. 8 A–C).

Following NMO, the traces within each CIP bin were stacked using a coherent stacking algorithm implemented in RADEX PRO, designed to enhance reflection continuity by summing traces with consistent phase and amplitude alignment while suppressing incoherent noise. This procedure does not involve semblance weighting but applies a local coherence threshold of 25% to exclude noisy traces. The clear alignment of reflection events and high signal coherence achieved through this stacking demonstrate the effectiveness of the CIP framework in organizing traces and producing a meaningful seismic image (Fig. 8D).

To further improve interpretability, a post-stack processing sequence was applied. This included a 1–10 Hz bandpass filter to suppress residual noise, horizontal coherence filtering (3 traces, 250 ms window) to enhance lateral continuity, automatic gain control (AGC) with a 500 ms window to balance amplitudes, and F-X interpolation at 50 m spacing to regularize trace density. Traces with offsets greater than 500 m were muted to reduce geometric bias. Finally, the time-domain seismic section was converted to depth using the composite velocity model adopted in prior stages (Fig. 9).

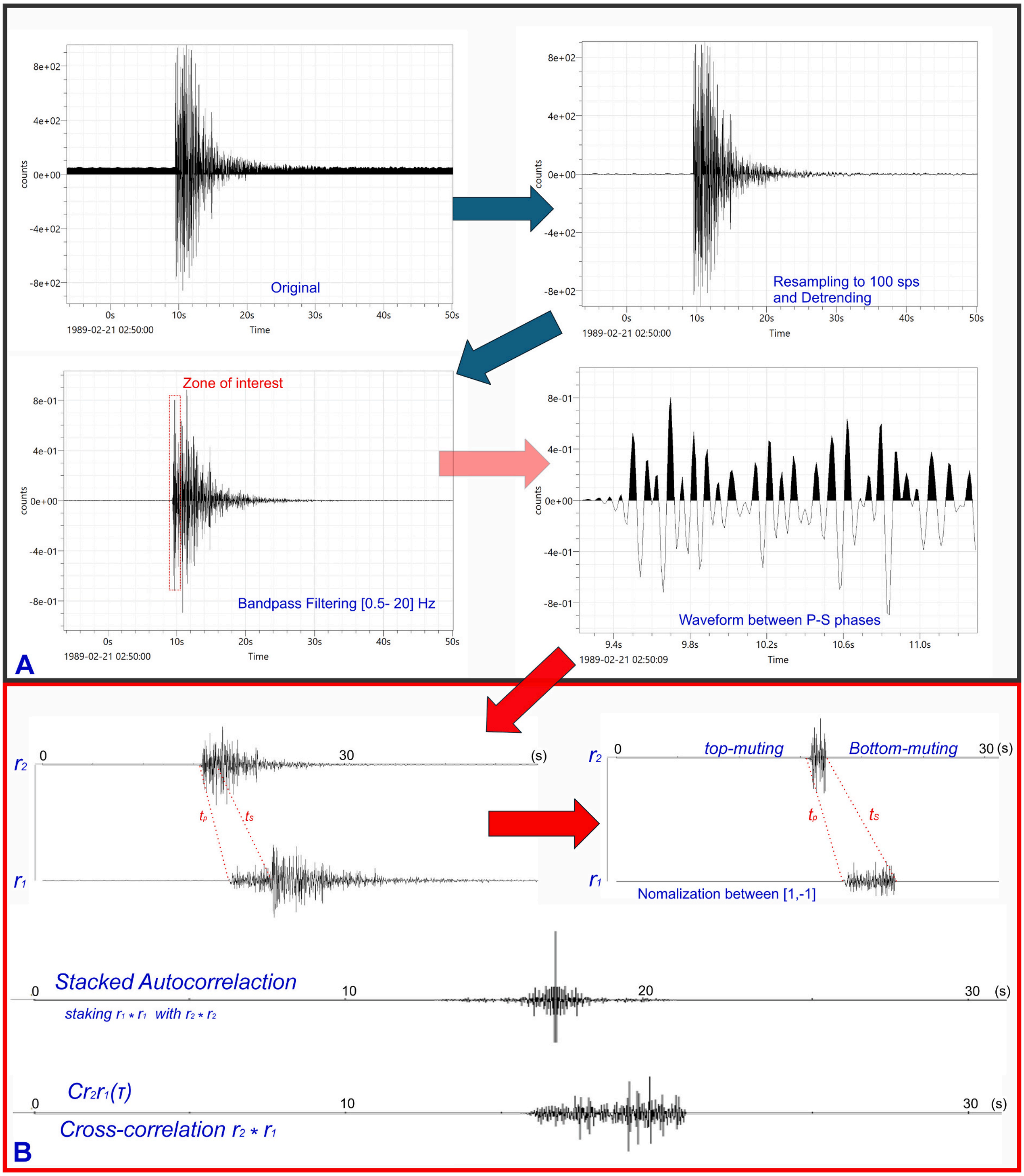

Fig. 4. (A) Example of an earthquake record at station r2 (ACHM, Chimeneas) illustrating the main preprocessing steps applied in Stage 1. From top to bottom: original waveform; waveform after resampling to 100 Hz and detrending; bandpass-filtered waveform (0.5–20 Hz) highlighting the zone of interest; and the extracted waveform segment between the P- and S-wave arrivals prior to amplitude normalization, used for interferometric processing. The apparent disappearance of the baseline signal after detrending reflects a plotting effect associated with waveform centering and amplitude scaling, rather than the removal of noise. (B) Example of waveforms recorded at stations pair r_1 and r_2 for a common earthquake. The traces are shown after isolation of the P—S window and amplitude normalization between -1 and 1 (Stage 1), followed by the corresponding autocorrelation and cross-correlation results used in Stage 2 of the interferometric workflow.

5. Results

5.1. 2D cross-section and seismotectonic data

The seismic interferometry profile provides coverage over a 21 km long section in the central part of the Granada Basin (Fig. 10). Panel A shows the broader seismotectonic framework along the profile direction (Stich et al., 2024), as well as the depth of the sediment-basement interface inferred by Araque-Pérez et al. (2025). Panel B illustrates the integration of the interferometry image displayed in amplitude mode into the previously proposed seismogenic model. The seismogenic model is based on instrumental seismicity data along a SW–NE transect across the GB (see relocated seismicity in Fig. 10). The main concentration of earthquakes occur in the NE portion of the transect at shallow depths—typically between 1 and 7 km—within the Sierra Elvira half-*graben*, bounded laterally by the Santa Fe Fault (SFF) and the Ermita Tres

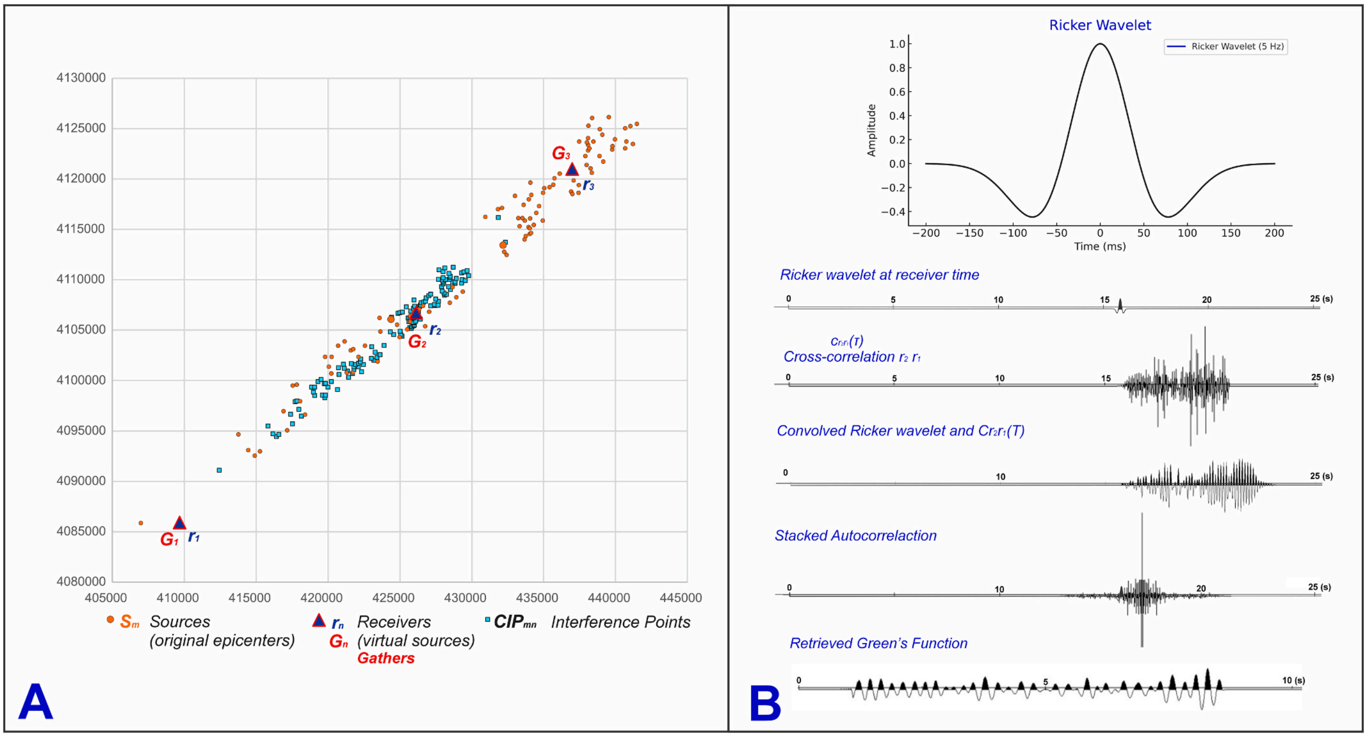

Fig. 5. (A) Location of the earthquakes and seismic stations used in the interferometry experiment. Common Interferometry Points (CIPs), shown as small blue squares, represent the surface locations where virtual seismic traces were constructed, indicating coverage and trace distribution for each receiver pair. (B) Implementation of the seismic interferometry equation (Eq. 2). Empirical Green's functions of Eq. 1 are discretely retrieved between each station considering their corresponding CIP. Then these functions are convolved with a 5 Hz zero-phase Ricker wavelet placed at the real station location. The resulting empirical Green's function is deconvolved using the stacked autocorrelation of the original signals to attenuate residual source effects. (For interpretation of the references to colour in this figure legend, the reader is referred to the web version of this article.)

Juanes Fault (ETJF).

At greater depths, the hypocentres align near 11 km along a low-angle southwest-dipping structure interpreted as a BD, with an estimated dip of approximately 5 degrees. This detachment hosts moderate-magnitude events, including a well-defined cluster (C06) situated between the Malahá fault (MF) and the BD, as well as another smaller cluster (C04) approximately 7 km further to the southwest, both aligned along the same detachment surface. Further SW, the principal structure if the Zafarrayas Fault (ZAF), showing steep, antithetic dip in NE direction. The ZAF is located among low-magnitude seismicity in the Mw 1.5–2.5 range, although it has historically been associated with the destructive 1884 Andalusian earthquake (e.g., Reicherter et al., 2003). Beneath the projection of ZAF fault, Stich et al. (2024) suggests a potential termination of the BD; however, its geometry remains unresolved and should be regarded as interpretative. Taken together, the model proposed by Stich et al. (2024) depicts a tectonic framework dominated by major SW-dipping fault systems, accompanied by synthetic and antithetic secondary structures. These were interpreted through hypocentral cluster analysis and provide a structural baseline for comparison with the interferometric results obtained in the present study. The interferometry section provides information for the central sector, characterized by low angle structures (associated to the detachment horizon) and high-angle structure (e.g. Malahá Fault).

5.2. *Interpretation of seismic interferometry section*

The interferometry sections presents several coherent and laterally continuous reflectors to be associated with the basement architecture. The sediment-basement interface inferred by Araque-Pérez et al. (2025) is expressed as a continuous reflector and correlates well with the uppermost seismic signal. Overlying this boundary are the Neogene sediments of the GB. The MF fault intersects a break in the seismic reflectors, further supporting its identification as a fault zone.

Two outstanding basement reflectors are identified in the seismic image. The first, R2, is observed between 12 and 20 km of lateral distance (*offset*) and lies at depths of approximately 7 to 10 km. This reflector dips toward the northeast. The second reflector, R1, appears at similar lateral positions but at depths exceeding 11 km. It exhibits a more disrupted geometry, potentially indicative of faulting consistent with structural features inferred by Stich et al. (2024). Seismic facies between R1 and R2 in Fig. 11 are characterized by lower reflectivity and may represent distinct geological units. Below R1, the incorporation of the BD proposed by Stich et al. (2024) is noted. Earthquakes located between R1 and the BD, mostly within the Mw 2–3 range, are interpreted as being associated with mechanical coupling or fault convergence along the BD.

To interpret further details of the seismic profile, we present the interpreted section in both trace and amplitude modes (Fig. 11, left and right panels, respectively), based on the identification of seismic units and major faults previously introduced in the preceding subsection. Travel-time to depth conversion was performed using the near-surface velocity model proposed by Araque-Pérez et al. (2025), complemented with the velocity models for the GB (Serrano, 1999; Serrano et al., 2024), with uncertainties estimated to be within 1.2 km at 15 km depth. The seismic sections reach an approximate depth of 17 km. While the resulting image contains noise and reflector discontinuity inherent to passive seismic methods, several coherent features allow for a robust structural interpretation. The main structures imaged along the transect are described in the following.

5.2.1. *Unit 1 (U1)*

Displayed in blue in the amplitude-mode seismic section, Unit U1 forms a lower crustal package (blue zone in the right panel) bounded at the top by reflector R1 (blue line in the left panel). This unit is

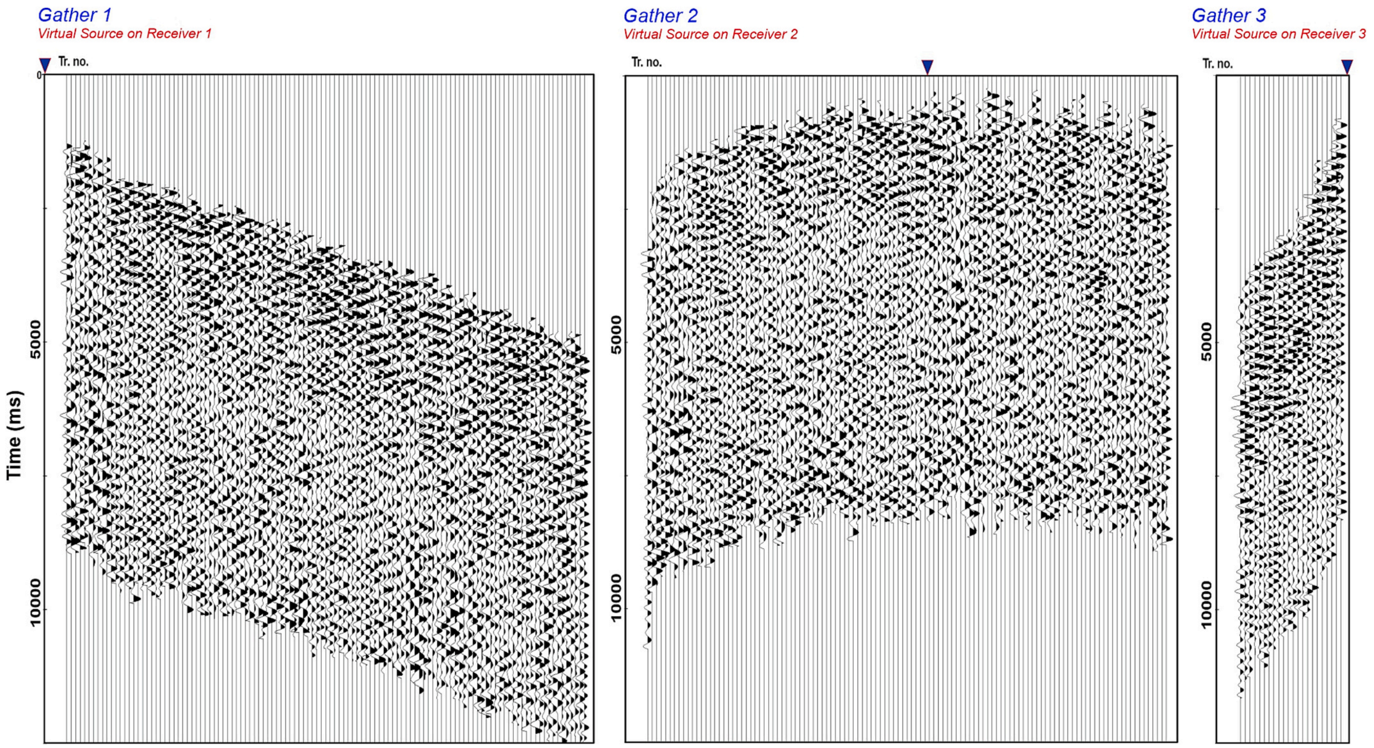

Fig. 6. Virtual source gathers constructed from the interferometric responses. Each gather (G1–G3) corresponds to one real seismic station acting as a virtual source. All individual empirical Green's functions are displayed prior to stacking; each trace corresponds to a single CIP. Traces are ordered laterally according to the surface position of their associated CIP. At this stage, only a preliminary geometric time-reference shift based on the theoretical P-wave travel time from the virtual source to the CIP has been applied. No static or normal moveout (NMO) corrections have been applied at this stage. (For interpretation of the references to colour in this figure legend, the reader is referred to the web version of this article.)

interpreted as a transitional zone between ductile and brittle crustal domains, partially outlined by the BD (dashed blue line). Major fault systems (sky blue lines) in the GB, including the MF, near the Chimeneas depocentre, and the Escúzar Fault (ESZ), north of the Cacín valley, appear to converge into this unit and root in the BD. These faults define a *graben*-like geometry that reflects the extensional kinematics of the basin within the imaged profile sector. The rupture and facies change observed along reflector R1 beneath the R. Cacín valley complicate its southwestward tracing. The upper portion of U1 shows a more brittle behaviour, while the deeper part, especially beneath the hypothetical BD, likely exhibits increased ductility.

5.2.2. Unit 2 (U2)

Unit U2 (highlighted in green in Fig. 11) is bounded by reflector R2 at the top and R1 at the base. It reaches a thickness of approximately 8 km in the SW sector and wedges out toward the NE to around 1.5 km. The unit exhibits a mean dip of 9 degrees to the northeast. Seismically, it hosts mostly low-magnitude events (around Mw 1.5). The geometry of its reflectors indicates sub-horizontal layering disrupted by major faults (sky blue lines) that converge into Unit U1. Reflector R2 is also intersected by an intermediate fault system (light green lines), which affects the overlying Unit U3.

From a geological perspective, Unit U2 may represent remnants of the Tethys–Iberia palaeomargin (e.g., Morales et al., 2022), or correlate with metamorphic complexes such as the Nevado, Filábride or Maláguide units. A weaker internal reflector (Ra, light purple zone in the left panel, and dashed green line in the right one) is observed within this unit and may represent a mechanically distinct subunit. The faults identified within U2 suggest that this unit plays a secondary structural role in the basin, possibly accommodating interaction between deeper deformation and the extensional regime in a synthetic mode—consistent with the *graben* formed by the overlying master faults.

5.2.3. Unit 3 (U3)

Unit U3 overlies U2 and is capped by the sedimentary basement (red line). Although this unit is largely aseismic (compare Fig. 10), the seismic section reveals several internal reflectors that are disrupted by fault systems (highlighted by yellow lines in Fig. 11), particularly in the upper-central portion of the unit. This configuration suggests significant stress accumulation and brittle deformation, constrained between MF and antithetic structures such as ESZ, and spatially coinciding with some of the newly identified faults (NIFs) proposed by Araque-Pérez et al. (2025) (see Fig. 1A). North of the MF, a fractured reflector (Rc, magenta zone in the left panel and yellow dashed line in the right one) is identified at approximately 6 km depth within a raised basement block (RB), interpreted as a *horst* structure. This reflector breaks normally across the MF and extends southwestward within Unit U3. Geologically, U3 may correspond to the Alpujárride Complex of the Internal Betic Zone (IBZ), situated in the footwall of MF. This unit thins toward the southwest and thickens to the northeast.

5.2.4. Unit 4 (U4)

This uppermost unit corresponds to the Neogene sediments of the GB. It is not clearly resolved in the section due to the limited bandwidth of the seismic data (1–10 Hz), which restricts resolution within the shallow sedimentary layers.

5.2.5. Fault systems

Faults have been detected according to the interruptions produced on the unit interfaces and internal reflectors. The analysis is further complemented as follows:

- Major Fault Systems: Two principal faults (sky blue lines), MF and ESZ, extend from Unit U1 to the upper part of U4, approaching the near-surface layers but without outcropping at the top of the profile.

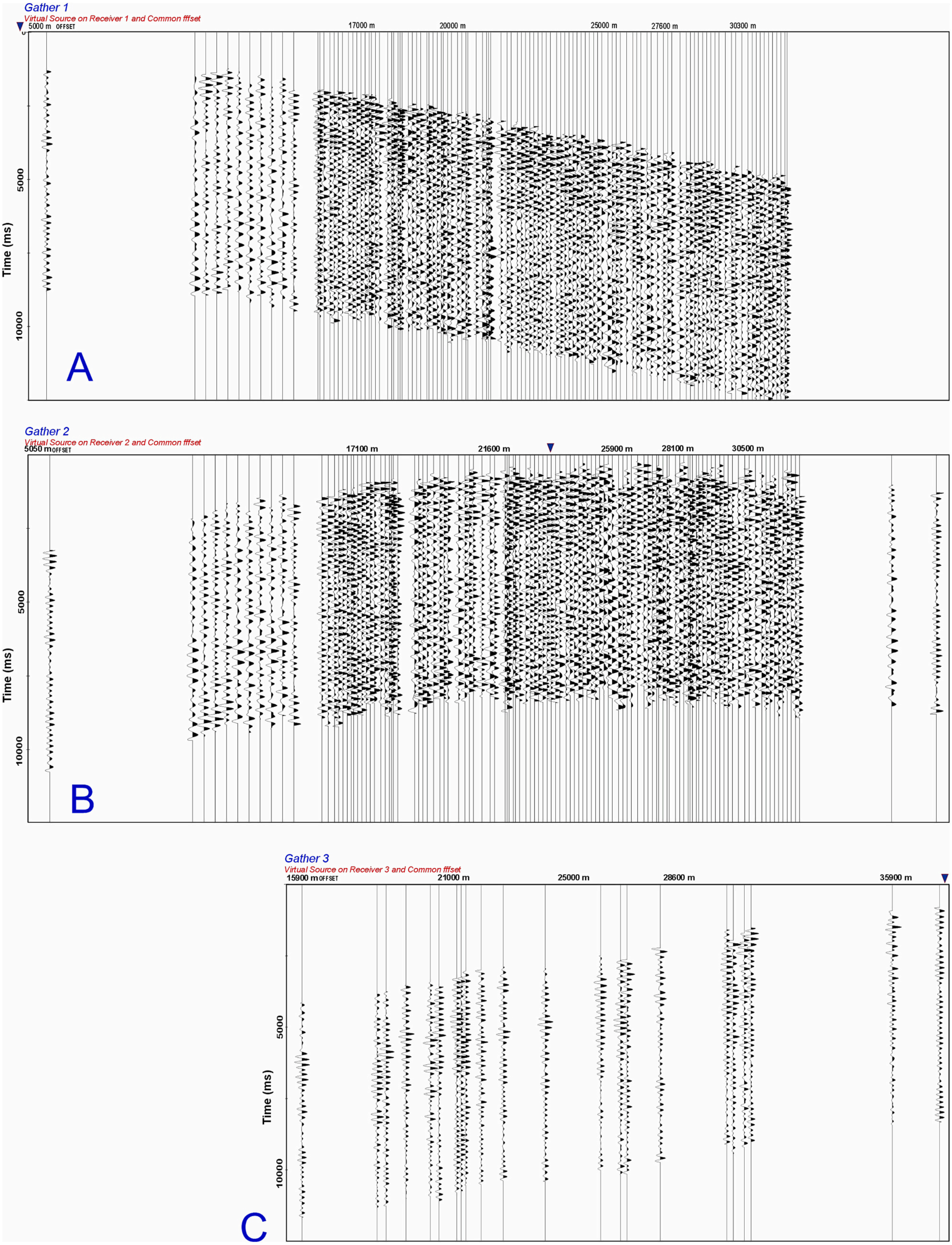

Fig. 7. (A, B, C) Empirical Green's functions are sorted by CIP and absolute offset from the virtual source r₁, without NMO corrections, depicting the data structure prior to stacking for each gather.

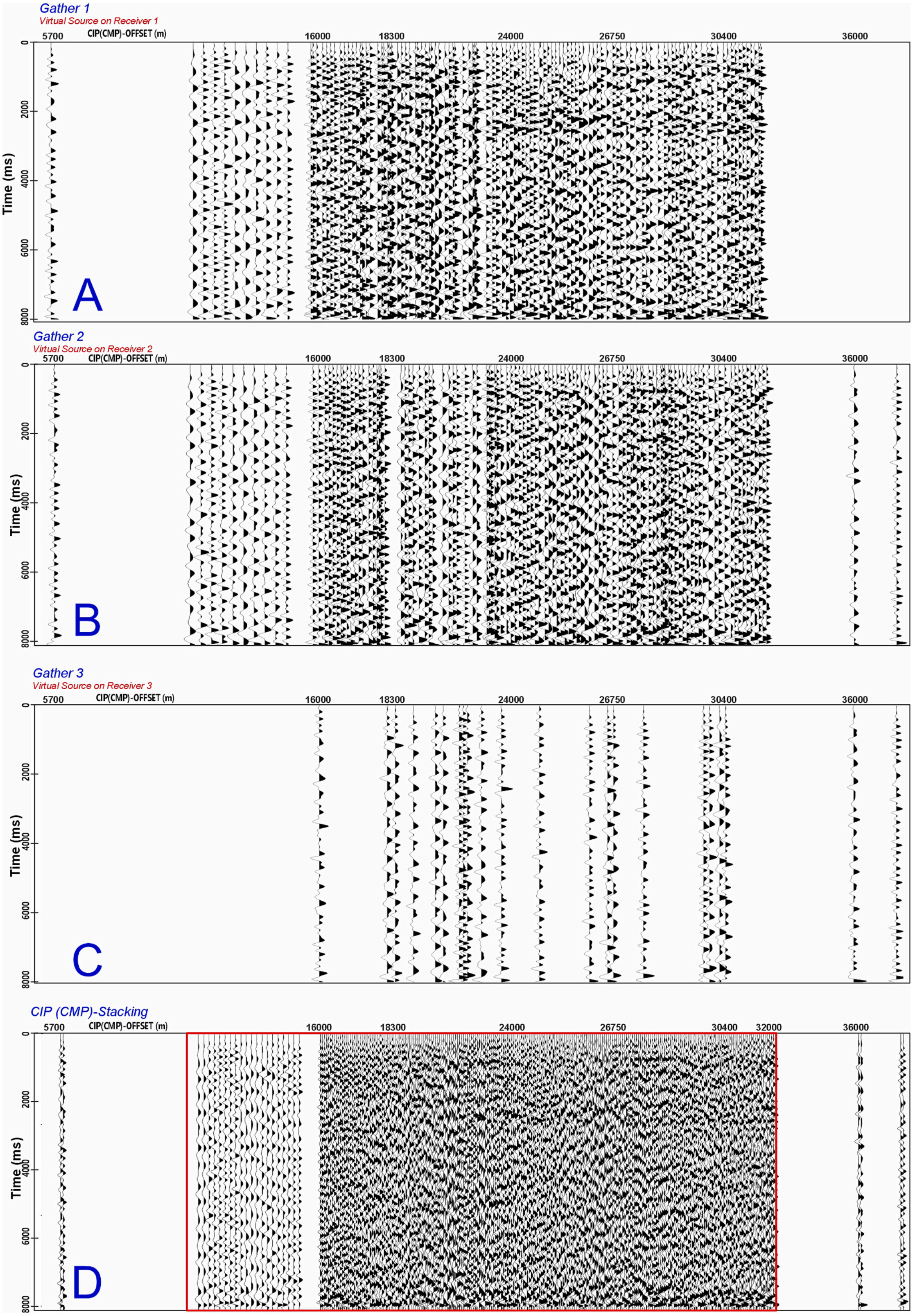

Fig. 8. (A, B, C) NMO correction of each gather sorted by CIP based on absolute offset from r_1. (D) Final stacked seismic interferometry section obtained using a coherent stacking algorithm implemented in RADEX PRO. The red rectangle highlights the segment with the most consistent spatial coverage, excluding traces beyond the reliable offset range.

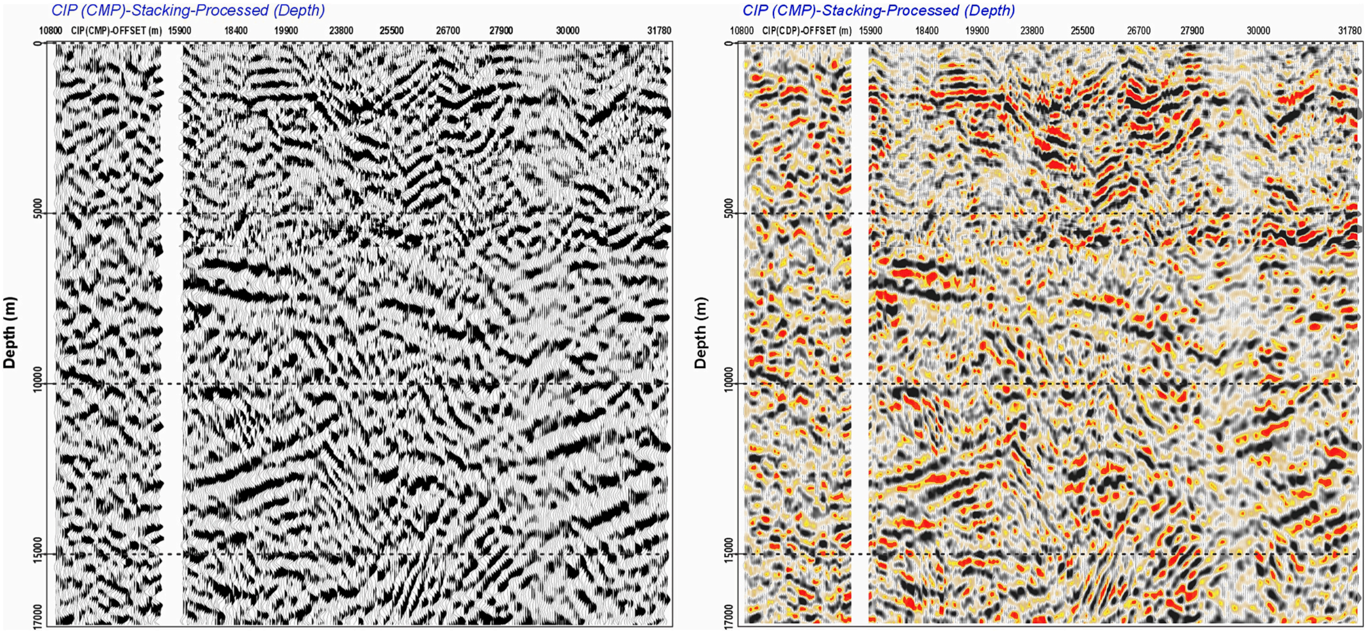

Fig. 9. Final seismic interferometry section after post-stack processing and depth conversion. The image displays the results in two formats: trace mode (left) and amplitude mode (right), providing complementary views of subsurface reflectivity.

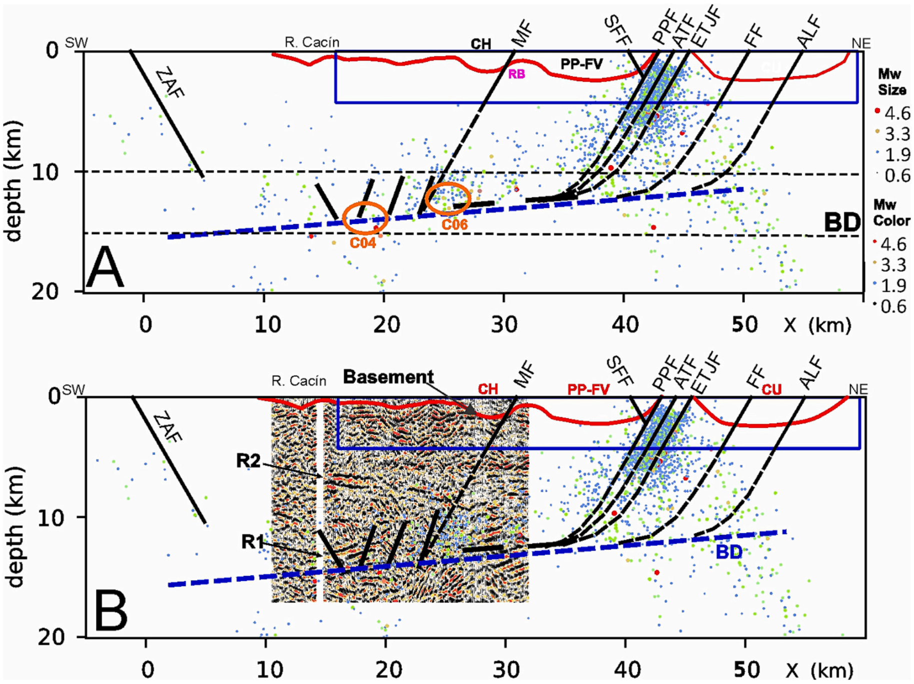

Fig. 10. (A) Seismogenic model–with the seismic clusters C04 and C06–proposed by Stich et al. (2024), overlaid with earthquakes hypocenters and the surface sedimentary basement model (Araque-Pérez et al., 2025). (B) Seismic interferometry profile in amplitude mode, highlighting the seismogenic zone shown in panel A. The blue rectangle indicates the near-surface model area (Araque-Pérez et al., 2025). Depocenters: CH, Chimeneas, PP-FV, Pinos Puente–Fuente Vaqueros; CU, Cubillas. RB: Uplifted basement block. Faults: MF, Malaha; ESZ, Escuzar; SF: Santa Fe; PPF, Pinos Puente; ATF, Atarfe; ETJF, Ermita Tres Juanes; FF, El Fargue; ALF, Alfacar. BD: Basal Detachment. (For interpretation of the references to colour in this figure legend, the reader is referred to the web version of this article.)

Their geometry suggests an antithetic Riedel configuration, which may define a *graben*-like structure broadly aligned with the Sierra Elvira half-*graben*. These faults terminate near the BD and correlate with seismic clusters C04 and C06 at the intersection between high-angle faults and the detachment (Stich et al., 2024). These structures highlight the underlying kinematics that may explain the current basin configuration.

- Intermediate Fault Systems: This set of faults (light green lines), with dips between 60 and 70 degrees, originates within Unit U2 and propagates upwards into Unit U3. These faults are synthetic to the major systems and may mediate stress transfer between deeper and shallower levels, resembling the geometries of the principal faults.
- Surface Fault Systems: A series of shallower faults (yellow lines) disrupt the reflectors within Unit U3, forming *horst* and *graben*

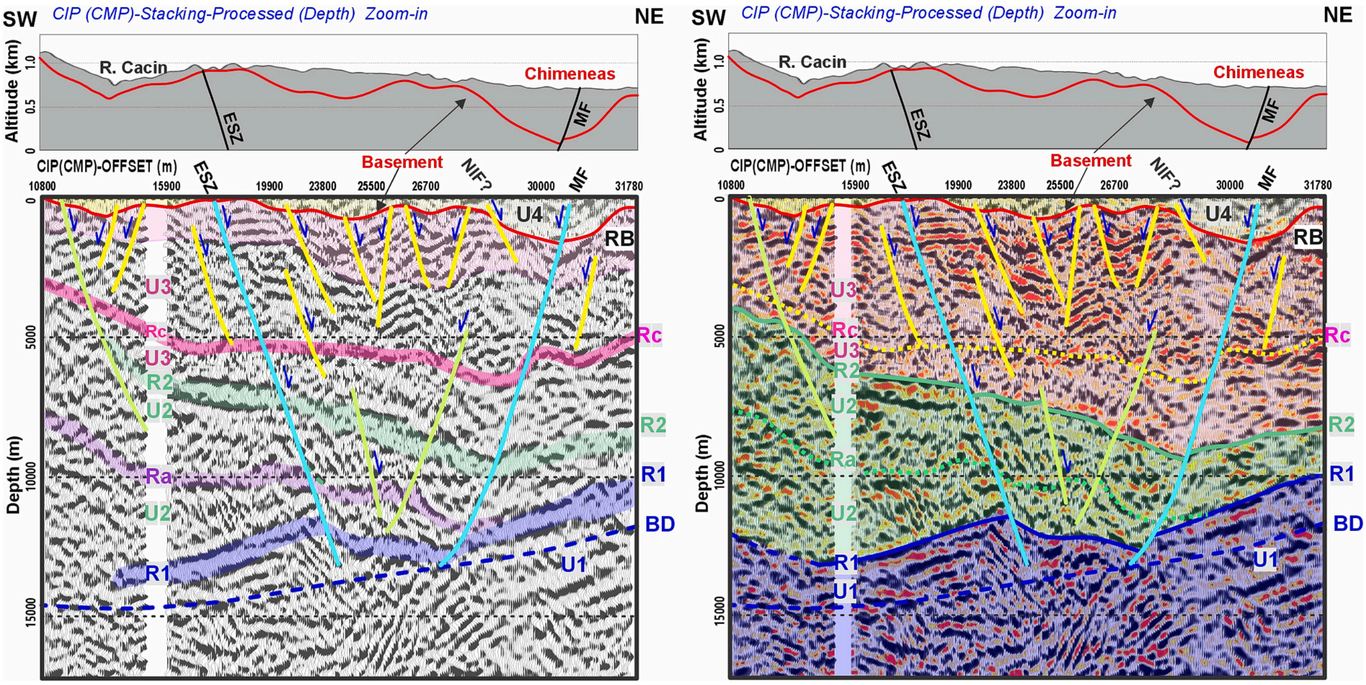

Fig. 11. Interpretation of the seismic interferometry section–in trace and amplitude modes (left and right panels). RB: Uplifted basement block. Faults: MF, Malahá Fault; ESZ, Escúzar Fault; NIF, New Identified Faults in prior research (e.g., Araque-Pérez et al., 2025). BD: Basal Detachment. Seismic reflectors: R1, R2, Ra, and Rc. Seismic units: U1, U2, U3, and U4.

structures. Some of these faults do not breach the sedimentary basement but likely represent a mechanical response to deeper fault-driven extension. Another of these faults propagate through the upper 5 km of the basin. One such fault—the NIF in the Chimeneas depocentre—extends into Unit U4 and functions as an antithetic Riedel to the MF fault. These systems are consistent with faulting patterns observed in reflection seismic profiles across the GB (Morales et al., 1990; Rodríguez-Fernández and Sanz de Galdeano, 2006; Araque-Perez, 2024).

5.3. Resulting model

The structural interpretation of the interferometric seismic section, the distribution of relocated hypocenters and the seismotectonic cross-section of the GB can be integrated into a coherent model, as illustrated in the AA' structural profile (Fig. 12). The distribution of seismicity with Mw magnitudes above 2 shows clear correlation with the major fault systems identified in the section, extending from the ALF fault in the northeast to the ZAF fault in the southwest. Notably, a

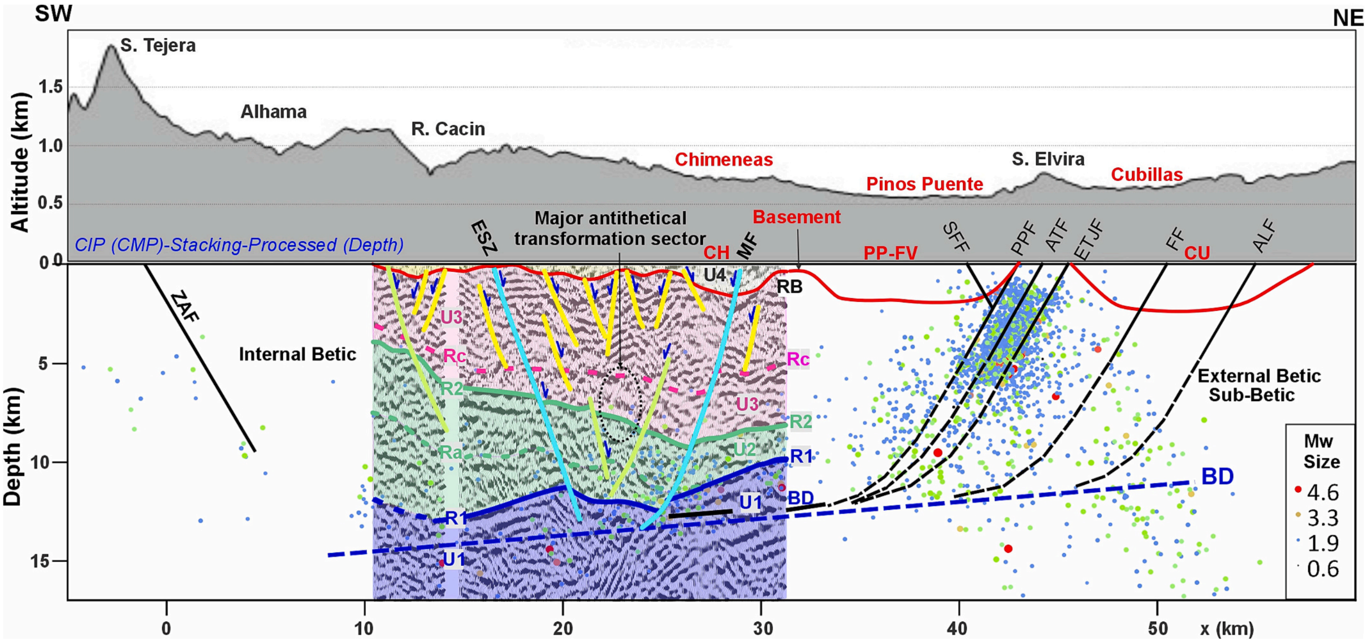

Fig. 12. Structural section derived from the deep interferometric model, incorporating 3D moment magnitudes (Mw) and the interpreted 2D seismic profile. Depocenters: CH, Chimeneas, PP-FV, Pinos Puente–Fuente Vaqueros; CU, Cubillas. RB: Uplifted basement block. Faults: MF, Malaha; ESZ, Escuzar; SF: Santa Fe; PPF, Pinos Puente; ATF, Atarfe; ETJF, Ermita Tres Juanes; FF, El Fargue; ALF, Alfacar. BD: Basal Detachment.

concentration of mid-crustal events is observed between 10 and 50 km horizontal distance, coinciding with the BD. Toward the distal ends of the profile—beyond the ZAF and ALF structures—both seismicity and magnitude decrease, which may reflect changes in the prevailing tectonic regime.

The interferometric seismic section is located between 11 km and 32 km along the profile, as this zone had the major CIP coverage. As previously discussed, the MF and ESZ faults, clearly imaged throughout the section, serve as key structural markers, along with the continuity of reflectors R1 and R2, in defining seismic units and tracing the geometry of fault systems. This joint interpretation supports the following observations:

- Unit U1 is closely associated with BD in their upper part. Within this unit the apparent termination of the main fault systems in above the BD is observed, particularly beneath reflector R1, marking a brittle ductile transition within the crust.
- Unit U2 contains a secondary internal reflector, Ra (green dashed line in Fig. 12), that marks a subtle change in seismic facies, separating two subunits with similar internal structure. The lower subunit tapers out against the MF fault, while both subunits display moderately chaotic reflectivity. Seismicity is distributed across the entire unit, though a slight decrease in Mw s is observed toward the top of U2 (around Mw 1.5–2.0), particularly near the contact with Unit U3.
- Unit U3 is bounded at its top by the sedimentary basement and displays internal segmentation. A lower subunit, bounded by reflector Rc (magenta dashed line in Fig. 12), shows distinct seismic facies and corresponds to a region of lower–or scarse–seismicity. Above this level, truncated and displaced reflectors indicate faults in a *horst–graben* configuration. These structures are consistent with fault systems observed in the upper 5 km Sanz de Galdeano et al. (e.g., 2003); Rodríguez-Fernández and Sanz de Galdeano (e.g., 2006); Araque-Pérez et al. (e.g., 2025) and appear to propagate into the overlying Unit U4.
- The major fault systems identified in the section, including the MF and ESZ faults, display steep dips and propagate upward through Unit U4. Around 22 km horizontal distance (x direction), a change in fault dip direction is observed, marking a transition from synthetic to antithetic faulting. This antithetic system is mostly confined between Units U2 and U3 and coincides with a zone of reduced seismic magnitudes. The region of dip polarity change (indicated by the black dashed ellipse in Fig. 12) corresponds to the termination of a major synthetic fault and the emergence of several antithetic structures.

6. Discussion

The seismic section was constructed using data from seismic stations aligned along the transect and from earthquakes located over the past 40 years by IAG-UGR. The selected high-quality location data correspond to RMS errors lesser than 0.3, underscoring the critical role of the local seismic network in elaborating a detailed earthquake catalogue. Achieving a coherent interferometric profile from a sparse dataset was possible thanks to the geometric re-organization of interferometric traces using the CIP construction, applied here as a practical aid. The profile reveals a prominent sub-horizontal reflector located between 10 and 15 km depth, beneath the ~2 km thick sedimentary cover (Morales et al., 1990; Rodríguez-Fernández and Sanz de Galdeano, 2006). This reflector spatially coincides with the BD previously inferred from hypocentral clustering analyses (Stich et al., 2024), and likely marks a compositional and rheological boundary within the upper crust. The agreement between the reflector and the distribution of seismicity suggests that this level functions as a tectonic decoupling zone, potentially associated with mineralogical or lithological contrasts that promote ductile behaviour.

6.1. Methodological implications of the CIP

Being conceptually analogous to the CDP approach in conventional reflection seismology (e.g., Yilmaz, 2001) and to certain interferometric stacking schemes (e.g., Schuster, 2009), the CIP served as a way to optimize subsurface illumination and spatial alignment of arrivals, thereby enhancing the continuity of the imaged structures. The analogous behaviour of CIP and CDP-like constructions resides in its stacking, which reinforces the coherence of P—P reflections (Yilmaz, 2001). At the same time, its geometry resembles the CCP approach in receiver function studies (e.g., Zhu and Kanamori, 2000), because the CIP location depends on the relative earthquake–receiver configuration rather than a simple midpoint. Importantly, no phase conversion is assumed: the interferometric workflow emphasizes the time window between the direct P arrival and the S phase, where the dominant contribution is from coherent P—P energy. Converted phases may be present within this interval, but they remain incoherent and are attenuated by stacking. In this sense, the CIP can be regarded as a practical adaptation of the CDP principle to the irregular geometries inherent to earthquake-based interferometry, enabling deep imaging even with sparse seismic networks.

6.2. Geological implications of the Basal Detachment (BD)

The BD, located at depths of 10–15 km, is expected to be located near the transition between the brittle upper crust and the underlying ductile crustal levels. This structural level may coincide with pre-Triassic lithologies that exhibit rheological contrasts associated with increasing pressure–temperature conditions at depth. Similar decoupling horizons have been documented in other Mediterranean basins, such as Sorbas and Lorca, where detachment levels are spatially correlated with metamorphic transitions and zones of enhanced ductility (García-Veigas et al., 2013; Martínez-Martínez et al., 2006). In accordance with this idea, deformation in Units U2 and U3 localises along steeply dipping normal faults that propagate up toward the surface, while no such behaviour has been identified within Unit U1, supporting a more ductile behaviour. This mechanical decoupling allows upper crustal faults to concentrate extensional strain, while deeper deformation is absorbed along the BD, thus facilitating the development of surface-breaching extensional structures.

Analogue models have confirmed that high-angle normal fault systems, often observed in extensional contexts, are associated with BD zones located at ductile–frictional boundaries (Ventisette et al., 2006). A similar tectonic decoupling process has been described in the Gulf of Corinth, where slip along an active BD at 9–11 km depth induces high-angle normal faults in the upper crust (Exadaktylos et al., 2003). Comparable extensional detachment systems have also been documented in the extensional domain of the Italian Apennines (Michele et al., 2020; Waldhauser et al., 2021; Lavecchia et al., 2021) and in southern Italy within the Calabrian arc (Brozzetti et al., 2017; Cirillo et al., 2022), where similar rheological boundaries control the localization of faulting. In particular, they act as basal detachments, defined as master detachment faults, along which high-angle fault systems nucleate, capable of generating strong earthquakes and reaching the surface, where morphological evidence is clearly observable (Cirillo et al., 2025).

6.3. Deep basal detachment and its relationship with surface structure

The BD is interpreted as a mechanically decoupled structure that accommodates deformation through a combination of aseismic creep and low-magnitude seismicity. While we currently cannot image the creep process directly, the reflector geometry and subdued seismicity beneath R1 suggest a ductile transition where strain may accumulate aseismically. In particular, a constant event production rate in earthquake clusters located near the BD support their embedment in a steady state creep process (Stich et al., 2024). Similar mixed-mode behaviour has been described in other tectonic settings, such as the Western Alps, where deep detachment levels play a key role in transferring stress from the ductile lower crust to overlying brittle fault systems (Schmid et al., 1996; Chertova et al., 2014). This dual behaviour reflects the transitional rheology expected near the brittle–ductile boundary and is critical for understanding the linkage between deep-seated structures and surface deformation.

In this tectonic scenario, activity of the BD appears to manifest through two complementary processes:

- Tectonic Creep: The continuous slip along the BD redistributes stress toward upper crustal normal faults (Lavier et al., 2013; Thom and Kirkpatrick, 2023), facilitating the development of *horst*-and-*graben* systems that characterize the basin's extensional architecture.
- Associated Seismicity: Moderate seismicity (Mw ~ 2–3) has been recorded at depths of 5 to 15 km, coinciding with the BD zone and the roots of major fault systems. These events likely reflect localised stress accumulation and rupture, particularly in sectors where fault orientations rotate toward sub-horizontal geometries (Stich et al., 2024).

The interpretation presented in this work suggests that the BD acts as a key structural controller in the basin, as evidenced by its correlation with fault geometry and seismic activity described in previous sections.

6.4. Comparison with regional seismic tomography

To assess the reliability of the structural interpretation derived from our seismic interferometric imaging, we conducted a comparison with the regional tomographic model recently published by Serrano et al. (2024). Their model, based on the joint inversion of P- and S-wave arrival times from 7051 earthquakes recorded by the local seismic network of IAG-UGR during the 2020–2021 Atarfe–Santa Fe seismic sequence (Morales et al., 2025), incorporates a total of 63,909 P phases and 32,987 S phases. This dataset enabled the generation of 3D distributions of P-wave velocity anomalies and Poisson's ratio across the GB, with a nominal vertical resolution of 2 km and a horizontal resolution of 2.2 km. The comparison of both approaches shows the consistency of several key features in the tomographic model and interferometric image. These include: (i) the geometry of the sedimentary infill and its lateral variations in the uppermost 3 km; (ii) the imaging of a *graben* structure between the Escúzar and Malahá faults; and (iii) the identification of a crustal-scale BD beneath the active fault system. The agreement between these independently derived models reinforces the robustness of our results and supports the tectonic interpretation proposed in this study. A more detailed comparative analysis, including the superposition of depth profiles and discussion of physical parameters, is provided in the Supplementary Material (Figure SP3).

7. Conclusions

A new seismic image of the Granada Basin (GB) was obtained by applying P-wave seismic interferometry to a sparse dataset of 117 local earthquakes recorded by three stations. A key methodological element was the use of CIPs, a practical geometric construction employed to organize the interferometric traces for stacking. This construction proved highly effective in producing a coherent image despite the limited data, demonstrating the remarkable capability of interferometric workflows to extract deep structural information from limited datasets. This method shows strong potential for application of passive seismic imaging in other structurally complex basins where dense seismic arrays or active-source surveys are unavailable.

The resulting seismic image, when integrated with the seismotectonic framework proposed by Stich et al. (2024), reveals a fault architecture rooted in a prominent low-angle reflector at depths of 10–15 km. This feature is interpreted as a basal detachment (BD), acting as a tectonic decoupling horizon between the brittle upper crust and deeper, more ductile levels. From this detachment, a system of normal faults propagates upward, generating *horst*-and-*graben* structures. These structures not only accommodate crustal extension but also influence the spatial distribution of seismicity and the tectono-sedimentary evolution of the Granada Basin. Overall, the integration of the AA′ seismic profile with both interferometric imaging and independent seismotectonic information provides a coherent and internally consistent structural model for the Granada Basin. The agreement between datasets reinforces the validity of the proposed interpretation and highlights the broader applicability of the methodology to deep imaging in other tectonically active or data-limited regions.

CRediT authorship contribution statement

C. Araque-Pérez: Writing – review & editing, Writing – original draft, Visualization, Validation, Resources, Methodology, Investigation, Formal analysis, Data curation, Conceptualization. **D. Stich:** Writing – review & editing, Visualization, Supervision, Investigation, Funding acquisition, Formal analysis. **T. Teixido:** Writing – review & editing, Supervision, Software, Project administration, Methodology, Investigation, Formal analysis, Data curation, Conceptualization. **E. Carmona:** Writing – review & editing, Validation, Resources, Methodology, Formal analysis, Data curation. **J. Morales:** Writing – review & editing, Visualization, Resources, Methodology, Investigation, Funding acquisition, Data curation. **F. Mancilla:** Writing – review & editing, Visualization, Supervision, Methodology, Funding acquisition.

Declaration of competing interest

The authors declare that they have no known competing financial interests or personal relationships that could have appeared to influence the work reported in this paper.

Acknowledgements

This research was supported by project PID2023-150188NB-I00 (Spanish Ministry of Science and Innovation), as well as by PID2019-109608GB-100: Estructura Litosférica y Deformación en las Béticas Orientales, and the program PTA2020-018650-I, all funded by the Spanish Ministry of Science and Innovation. We also thank I. Serrano Bermejo and M. A. Dengra for providing access to profile data from their 3D seismic tomographic model, which greatly assisted the comparison presented in the Supplementary Material. Funding for open access charge: Universidad de Granada / CBUA.

Appendix A. Supplementary data

Supplementary data to this article can be found online at https://doi.org/10.1016/j.tecto.2026.231114.

Data availability

All data used in this study can be obtained from the corresponding author upon reasonable request.

References

Agosta, F., Ruano, P., Rustichelli, A., Tondi, E., Galindo-Zaldívar, J., Sanz de Galdeano, C., 2012. Inner structure and deformation mechanisms of normal faults in conglomerates and carbonate grainstones (Granada basin, Betic cordillera, Spain): inferences on fault permeability. J. Struct. Geol. 45. https://doi.org/10.1016/j.jsg.2012.04.003.

Aki, K., Richards, P.G., 2002. Quantitative Seismology, Second edition. Univ. Science Books, Sansalito, CA, pp. 218–235 (ISBN 0-935702-96-2.).

Araña, Vegas, R., 1974. Plate tectonics and volcanism in the Gibraltar arc. Tectonophysics 24. https://doi.org/10.1016/0040-1951(74)90008-0.

Araque-Pérez, C., Mancilla, F.d.L., López-Comino, J.A., Stich, D., Morales, J., Teixido, T., 2025. New geological insights from legacy seismic sections: decoding the Granada Basin (Spain). Mar. Pet. Geol., 107294 https://doi.org/10.1016/j.marpetgeo.2025.107294.

Araque-Perez, C.J., 2024. Reevaluating soil amplification using multi-spectral HVSR technique in la Chana neighborhood, Granada, Spain. J. Seismol. 28, 921–949. https://doi.org/10.1007/s10950024-10227-2.

Azañón, J., García-Mayordomo, J., Insua, J., Rodríguez-Peces, M., 2013. Seismic hazard of the Granada fault. Cuat. Geomorfol. 27. https://hdl.handle.net/20.500.14352/34427.

Balanya, Garcia-Dueñas, 1987. Les directions structurales dans le domaine d'alborán de part et d'autre du détroit de gibraltar. C. R. Acad. Sci. Ser. II Mec. Phys. Chim. Sci. Univers Sci. Terre 304. http://pascal-francis.inist.fr/vibad/index.php?action=getRecordDetail&idt=8179331.

Benito, M.B., Navarro, M., Vidal, F., Gaspar-Escribano, J., García-Rodríguez, M.J., Martínez-Solares, J.M., 2010. A new seismic hazard assessment in the region of Andalusia (southern Spain). Bull. Earthq. Eng. 8. https://doi.org/10.1007/s10518-010-9175-9.

Bensen, G., Ritzwoller, M., Barmin, M., Levshin, A.L., Lin, F., Moschetti, M., Shapiro, N., Yang, Y., 2007. Processing seismic ambient noise data to obtain reliable broad-band surface wave dispersion measurements. Geophys. J. Int. 169, 1239–1260. https://doi.org/10.1111/j.1365246X.2007.03374.x.

Ben-Zion, Y., 2001. Dynamic ruptures in recent models of earthquake faults. J. Mech. Phys. Solids 49, 2209–2244. https://doi.org/10.1016/S0022-5096(01)00036-9.

Booth-Rea, G., Ranero, C.R., Grevemeyer, I., Martínez-Martínez, J.M., 2007. Crustal types and Tertiary tectonic evolution of the Alborán sea, western Mediterranean. Geochem. Geophys. Geosyst. 8. https://doi.org/10.1029/2007GC001639.

Brozzetti, F., Cirillo, D., Liberi, F., PiLuso, E., Faraca, E., De Nardis, R., Lavecchia, G., 2017. Structural style of quaternary extension in the Crati Valley (Calabrian arc): evidence in support of an east-dipping detachment fault. Ital. J. Geosci. 136, 434–453. https://doi.org/10.3301/IJG.2017.11.

Calvert, A., Sandvol, E., Seber, D., Barazangi, M., Roecker, S., Mourabit, T., Vidal, F., Alguacil, G., Jabour, N., 2000. Geodynamic evolution of the lithosphere and upper mantle beneath the Alboran region of the western Mediterranean: constraints from travel time tomography. J. Geophys. Res. Solid Earth 105. https://doi.org/10.1029/2000jb900024.

Campillo, M., Paul, A., 2008. Long-range correlations in the diffuse seismic coda. In: Seismic Interferometry: history and present Status. Society of Exploration Geophysicists. URL: doi:10.1190/1.9781560801924, doi:10.1190/1.9781560801924.

Carmona, E., 2009. Caracterización de sistemas de fractura mediante la localización relativa de terremotos tectónicos y volcánicos usando métodos clásicos y técnicas de array. URL: https://digibug.ugr.es/handle/10481/2724.

Carmona, E., Stich, D., Ibañez, J.M., Saccorotti, G., 2009. Multiplet focal mechanisms from polarities and relative locations: the Iznajar swarm in southern Spain. Bull. Seismol. Soc. Am. 99. https://doi.org/10.1785/0120090036.

Casas, J.A., Badi, G.A., Franco, L., Draganov, D., 2020. Seismic interferometry applied to regional and teleseismic events recorded at Planchón-Peteroa volcanic complex, Argentina-Chile. J. Volcanol. Geotherm. Res. 393, 106805. https://doi.org/10.1016/j.jvolgeores.2020.106805.

Chertova, M.V., Spakman, W., Geenen, T., Berg, A.P.V.D., Hinsbergen, D.J.V., 2014. Underpinning tectonic reconstructions of the western Mediterranean region with dynamic slab evolution from 3-D numerical modeling. J. Geophys. Res. Solid Earth 119. https://doi.org/10.1002/2014JB011150.

Cirillo, D., Totaro, C., Lavecchia, G., Orecchio, B., de Nardis, R., Presti, D., Ferrarini, F., Bello, S., Brozzetti, F., 2022. Structural complexities and tectonic barriers controlling recent seismic activity in the Pollino area (Calabria–Lucania, southern Italy) – constraints from stress inversion and 3D fault model building. Solid Earth 13, 205–228. https://doi.org/10.5194/se-13-205-2022.

Cirillo, D., Tangari, A.C., Scarciglia, F., Lavecchia, G., Brozzetti, F., 2025. UAV-PPK photogrammetry, GIS, and soil analysis to estimate long-term slip rates on active faults in a seismic gap of Northern Calabria (Southern Italy). Remote Sens. 17, 3366. https://doi.org/10.3390/rs17193366.

Claerbout, J.F., 1968. Synthesis of a layered medium from its acoustic transmission response. Geophysics 33, 264–269. https://doi.org/10.1190/1.1439927.

Cruz, M.D.R., Sanz de Galdeano, C., Lázaro, C., 2005. Metamorphic evolution of Triassic rocks from the transition zone between the Maláguide and Alpujárride complexes (Betic cordilleras, Spain). Eur. J. Mineral. 17, 81–91. https://doi.org/10.1127/0935-1221/2005/0017-0081.

Curtis, A., Halliday, D., 2010. Source-receiver wave field interferometry. In: Physical Review E—Statistical, Nonlinear, and Soft Matter Physics, 81, p. 046601. https://doi.org/10.1103/PhysRevE.81.046601. Phys. Rev. E.

Curtis, A., Gerstoft, P., Sato, H., Snieder, R., Wapenaar, K., 2006. Seismic interferometry—turning noise into signal. Lead. Edge 25, 1082–1092. https://doi.org/10.1190/1.2349814.

Curtis, A., Nicolson, H., Halliday, D., Trampert, J., Baptie, B., 2009. Virtual seismometers in the subsurface of the earth from seismic interferometry. Nat. Geosci. 2, 700–704. https://doi.org/10.1038/ngeo615.

Duggen, S., Hoernle, K., den Bogaard, P.V., Rüpke, L., Morgan, J.P., 2003. Deep roots of the Messinian salinity crisis. Nature 422. https://doi.org/10.1038/nature01553.

Exadaktylos, G., Vardoulakis, I., Stavropoulou, M., Tsombos, P., 2003. Analogue and numerical modeling of normal fault patterns produced due to slip along a detachment zone. Tectonophysics 376, 117–134. https://doi.org/10.1016/J.TECTO.2003.08.005.

Galetti, E., Curtis, A., 2012. Generalised receiver functions and seismic interferometry. Tectonophysics 532, 1–26. https://doi.org/10.1016/j.tecto.2011.12.004.

Galindo-Zaldívar, J., González-Lodeiro, F., Jabaloy, A., 1993. Stress and palaeostress in the Betic-Rif cordilleras (Miocene to the present). Tectonophysics 227, 105–126. https://doi.org/10.1016/00401951(93)90090-7.

Galindo-Zaldívar, J., Jabaloy, A., González-Lodeiro, F., 1996. Reaction of the Mecina detachment in the western sector of Sierra Nevada (Betic cordilleras, SE Spain). In: Comptes rendus de l'Académie des sciences. Serie 2. Sciences de la terre et des planètes, 323, pp. 615–622. http://pascal-francis.inist.fr/vibad/index.php?action=getRecordDetail&idt=3220668.

Galindo-Zaldívar, J., Jabaloy, A., Serrano, I., Morales, J., González-Lodeiro, F., Torcal, F., 1999. Recent and present-day stresses in the Granada basin (Betic cordilleras): example of a late Miocene-present-day extensional basin in a convergent plate boundary. Tectonics 18. https://doi.org/10.1029/1999TC900016.

García-Alix, A., Minwer-Barakat, R., Suárez, E.M., Freudenthal, M., 2009. Small mammals from the early Pleistocene of the Granada basin, southern Spain. Quat. Res. 72. https://doi.org/10.1016/j.yqres.2009.06.004.

Garcia-Castellanos, D., Villaseñor, A., 2011. Messinian salinity crisis regulated by competing tectonics and erosion at the Gibraltar arc. Nature 480, 359–363. https://doi.org/10.1038/nature10651.

García-Dueñas, V., Balanyá, J.C., Martínez-Martínez, J.M., 1992. Miocene extensional detachments in the outcropping basement of the northern Alboran basin (Betics) and their tectonic implications. Geo-Mar. Lett. 12, 88–95. https://doi.org/10.1007/BF02084917.

García-Veigas, J., Cendón, D.I., Rosell, L., Ortí, F., Ruiz, J.T., Martín, J.M., Sanz, E., 2013. Salt deposition and brine evolution in the Granada basin (late Tortonian, SE Spain). Palaeogeogr. Palaeoclimatol. Palaeoecol. 369. https://doi.org/10.1016/j.palaeo.2012.11.010.

Gil-Zepeda, S.A., Luzón, F., Aguirre, J., Morales, J., Sánchez-Sesma, F.J., Ortiz-Alemán, C., 2002. 3D seismic response of the deep basement structure of the Granada basin (southern Spain). Bull. Seismol. Soc. Am. 92. https://doi.org/10.1785/0120010262.

Lavecchia, G., de Nardis, R., Ferrarini, F., Cirillo, D., Bello, S., Brozzetti, F., 2021. Regional seismotectonic zonation of hydrocarbon fields in active thrust belts: a case study from Italy. In: Bonali, F.L., Mariotto, F.P., Tsereteli, N. (Eds.), Building Knowledge for Geohazard Assessment and Management in the Caucasus and Other Orogenic Regions. Springer, Dordrecht, pp. 89–128.

Lavier, L.L., Bennett, R.A., Duddu, R., 2013. Creep events at the brittle ductile transition. Geochem. Geophys. Geosyst. 14, 3334–3351. https://doi.org/10.1002/ggge.20178.

Lozano, L., Cantavella, J.V., Gaite, B., Ruiz-Barajas, S., Antón, R., Barco, J., 2022. Seismic analysis of the 2020–2021 Santa Fe seismic sequence in the Granada basin, Spain: relocations and focal mechanisms. Seismol. Res. Lett. 93. https://doi.org/10.1785/0220220097.

Luque-Espinar, J.A., Mateos, R.M., 2023. Hydrochemical changes in thermal waters related to seismic activity: the case of the 2020-2021 seismic sequence in Granada (S Spain). J. Hydrol. https://doi.org/10.1016/j.jhydrol.2023.130390.

Madarieta-Txurruka, A., Galindo-Zaldívar, J., González-Castillo, L., Peláez, J.A., Ruiz-Armenteros, A.M., Henares, J., Garrido-Carretero, M.S., Avilés, M., Gil, A.J., 2021. Highand low-angle normal fault activity in a collisional orogen: the northeastern Granada basin (Betic cordillera). Tectonics 40. https://doi.org/10.1029/2021TC006715.

Madarieta-Txurruka, A., González-Castillo, L., Peláez, J.A., Catalán, M., Henares, J., Gil, A.J., Lamas-Fernández, F., Galindo-Zaldívar, J., 2022. The role of faults as barriers in confined seismic sequences: 2021 seismicity in the Granada basin (Betic cordillera). Tectonics 41. https://doi.org/10.1029/2022TC007481.

Madarieta-Txurruka, A., Peláez, J.A., González-Castillo, L., Gil, A.J., Galindo-Zaldívar, J., 2023. Active collapse in the central Betic cordillera: development of the extensional system of the Granada basin. Appl. Sci. 13, 9138. https://doi.org/10.3390/app13169138.

Mancilla, F., Stich, D., Berrocoso, M., Martin, R., Morales, J., Fernandez-Ros, A., Paez, R., Perez-Pena, A., 2013. Delamination in the Betic range: deep structure, seismicity, and GPS motion. Geology 41, 307–310. https://doi.org/10.1130/G33733.1.

Mancilla, F., Booth-Rea, G., Stich, D., Pérez-Peña, J.V., Morales, J., Azañón, J.M., Martin, R., Giaconia, F., 2015. Slab rupture and delamination under the Betics and Rif constrained from receiver functions. Tectonophysics 663, 225–237. https://doi.org/10.1016/j.tecto.2015.06.028.

Martínez-Martínez, J.M., Booth-Rea, G., Azañón, J.M., Torcal, F., 2006. Active transfer fault zone linking a segmented extensional system (Betics, southern Spain): insight into heterogeneous extension driven by edge delamination. Tectonophysics 422, 159–173. https://doi.org/10.1016/j.tecto.2006.06.001.

Martin-Rojas, I., Alfaro, P., Galindo-Zaldivar, J., Borque-Arancón, M.J., García-Tortosa, F.J., Sanz de Galdeano, C., Avilés, M., Sánchez-Alzola, A., González-Castillo, L., Ruano, P., et al., 2023. Insights of active extension within a collisional orogen from GNSS (Central Betic cordillera, S Spain). Tectonics 42, e2022TC007723. https://doi.org/10.1029/2022TC007723.

Meijninger, B.M.L., 2006. Late-Orogenic Extension and Strike-Slip Deformation in the Neogene of Southeastern Spain. volume 269. Utrecht University. https://dspace.library.uu.nl/handle/1874/14037.

Michele, M., Chiaraluce, L., Di Stefano, R., Waldhauser, F., 2020. Fine-scale structure of the 2016–2017 Central Italy seismic sequence from data recorded at the Italian National Network. J. Geophys. Res. Solid Earth 125, e2019JB018440. https://doi.org/10.1029/2019JB018440.

Monie, P., Galindo-Zaldivar, J., Lodeiro, F.G., Gofee, B., Jabaloy, A., 1991. 40ar/39 AR-geochronology of alpine tectonism in the Betic cordilleras (southern Spain). J. Geol. Soc. Lond. 148, 289–297. https://doi.org/10.1144/gsjgs.148.2.0289.

Morales, J., Vidal, F., Miguel, F.D., Alguacil, G., Posadas, A., Ibañez, J., Guzmán, A., Guirao, J., 1990. Basement structure of the Granada basin, Betic cordilleras, southern Spain. Tectonophysics 177, 337–348. https://doi.org/10.1016/0040-1951(90)90394-N.

Morales, J., Serrano, I., Vidal, F., Torcal, F., 1997. The depth of the earthquake activity in the central Betics (southern Spain). Geophys. Res. Lett. 24, 3289–3292. https://doi.org/10.1029/97GL03306.

Morales, J., Molina-Aguilera, A., de Lis Mancilla, F., Stich, D., Azañón, J.M., Teixidó, T., López-Comino, J.A., Heit, B., Yuan, X., Posadas, A.M., 2022. Preservation of the Iberian Tethys paleomargin beneath the eastern Betic mountain range. Gondwana Res. 106, 237–246. https://doi.org/10.1016/j.gr.2022.01.015.

Morales, J., Dengra, M.Á., López-Comino, J.Á., López-Abenza, P.J., Stich, D., Araque-Pérez, C., Cesca, S., Maestre, J., 2025. Fault identification, complexity and evolution of the 2021, Atarfe-Santa Fe earthquake swarm (Granada basin, Spain). Geophys. J. Int., ggaf132 https://doi.org/10.1093/gji/ggaf132.

Pedrera, A., Ruiz-Constán, A., Galindo-Zaldívar, J., Chalouan, A., Sanz de Galdeano, C., MarínLechado, C., Ruano, P., Benmakhlouf, M., Akil, M., López-Garrido, A.C., Chabli, A., Ahmamou, M., González-Castillo, L., 2011. Is there an active subduction beneath the Gibraltar orogenic arc? Constraints from Pliocene to present-day stress field. J. Geodyn. 52. https://doi.org/10.1016/j.jog.2010.12.003.

Pérez-Peña, J., Azañón, J., Azor, A., Booth-Rea, G., Galve, J., Roldán, F., Mancilla, F., Giaconia, F., Morales, J., Al-Awabdeh, M., 2015. Quaternary landscape evolution driven by slab-pull mechanisms in the Granada basin (central Betics). Tectonophysics 663, 5–18. https://doi.org/10.1016/j.tecto.2015.07.035.

QAFI, 2021. Quaternary faults database of Iberia. Instituto Geológico Minero de España (IGME). IGME-CSIC, España. https://info.igme.es/qafi/.

Reicherter, K.R., Jabaloy, A., Galindo-Zaldívar, J., Ruano, P., Becker-Heidmann, P., Morales, J., Reiss, S., González-Lodeiro, F., 2003. Repeated palaeoseismic activity of the Ventas de Zafarraya fault (S Spain) and its relation with the 1884 Andalusian earthquake. Int. J. Earth Sci. 92. https://doi.org/10.1007/s00531-003-0366-3.

Ricker, N., 1953. The form and laws of propagation of seismic wavelets. Geophysics 18. https://doi.org/10.1190/1.1437843.

Rodríguez-Fernández, J., Sanz de Galdeano, C., 2006. Late orogenic intramontane basin development: the Granada basin, Betics (southern Spain). Basin Res. 18, 85–102. https://doi.org/10.1111/j.1365-2117.2006.00284.x.

Rodríguez-Fernández, J., Fernández, J., Lopez-Garrido, A.C., de Galdeano, C., 1984. The central sector of the Betic cordilleras, a realm situated between the Atlantic and Mediterranean domains, during the upper Miocene. Ann. Géol. Pays Hellén. 32, 97–103. http://pascal-francis.inist.fr/vibad/index.php?action=getRecordDetail&idt=8788164.

Rosenbaum, G., Lister, G.S., Duboz, C., 2002. Reconstruction of the tectonic evolution of the western mediterranean since the Oligocene. J. Virtual Explor. 8. https://doi.org/10.3809/jvirtex.2002.00053.

Ruiz-Constán, A., Galindo-Zaldívar, J., Pedrera, A., Célérier, B., Marín-Lechado, C., 2011. Stress distribution at the transition from subduction to continental collision (northwestern and central Betic cordillera). Geochem. Geophys. Geosyst. 12. https://doi.org/10.1029/2011GC003824 n/a–n/a.

Sanz de Galdeano, C., Cruz, M.D.R., 2016. Late Paleozoic to Triassic formations unconformably deposited over the Ronda peridotites (Betic cordilleras): evidence for their Variscan time of crustal emplacement. Estud. Geol. 72, e043. https://doi.org/10.3989/egeol.42046.368.

Sanz de Galdeano, C., Andreo, B., Garcıa-Tortosa, F., López-Garrido, A., 2001. The Triassic paleogeographic transition between the Alpujarride and Malaguide complexes Betic–Rif internal zone (S Spain, N Morocco). Palaeogeogr. Palaeoclimatol. Palaeoecol. 167, 157–173. https://doi.org/10.1016/S0031-0182(00)00236-4.

Sanz de Galdeano, C., Pelaez Montilla, F., Lopez Casado, C., 2003. Seismic potential of the main active faults in the Granada basin (southern Spain). Pure Appl. Geophys. 160, 1537–1556. https://doi.org/10.1007/s00024-003-2359-3.

Sanz de Galdeano, C., Garcia-Tortosa, F., Pelaez, J., Alfaro, P., Azanon, J., Galindo-Zaldivar, J., et al., 2012. Main active faults in the Granada and Guadix-Baza basins (Betic cordillera). J. Iber. Geol. 38, 1–20. https://doi.org/10.5209/rev_JIGE.2012.v38.n1.39215.

Schmid, S.M., Pfiffner, O.A., Froitzheim, N., Schönborn, G., Kissling, E., 1996. Geophysical geological transect and tectonic evolution of the Swiss-Italian Alps. Tectonics 15, 1036–1064. https://doi.org/10.1029/96TC00433.

Schuster, G.T., 2009. Seismic interferometry. Cambridge University Press. https://doi.org/10.1017/CBO9780511581557.

Schuster, G.T., Zhou, M., 2006. A theoretical overview of model-based and correlation-based redatuming methods. Geophysics 71, SI103–SI110. https://doi.org/10.1190/1.2208967.

Serrano, I., 1999. Distribución espacial de la sismicidad en las Cordilleras Béticas-Mar de Alborán. Ph.D. thesis. Universidad de Granada.

Serrano, I., Dengra Martínez, M., Torcal Medina, F., Zhao, D., 2024. Azimuthal seismic anisotropy in the crust beneath the Granada basin (Spain). Tectonophysics. https://doi.org/10.1016/j.tecto.2024.230360.

Shapiro, N.M., Campillo, M., 2004. Emergence of broadband Rayleigh waves from correlations of the ambient seismic noise. Geophys. Res. Lett. 31. https://doi.org/10.1029/2004GL019491.

Shearer, P., 2009. Introduction to Seismology, 2nd edition ed. Cambridge University Press, Cambridge, UK. ISBN 978-0-521-70842-5, url: http://cambridge.org/Shearer. doi:10.1017/9781316877111.

Snieder, R., Hagerty, M., 2004. Monitoring change in volcanic interiors using coda wave interferometry: application to Arenal volcano, Costa Rica. Geophys. Res. Lett. 31. https://doi.org/10.1029/2004GL019670.

Snieder, R., Wapenaar, K., Larner, K., 2006. Spurious multiples in seismic interferometry of primaries. Geophysics 71, SI111–SI124. https://doi.org/10.1190/1.2211507.

Stich, D., Ammon, C.J., Morales, J., 2003. Moment tensor solutions for small and moderate earthquakes in the Ibero-Maghreb region. J. Geophys. Res. Solid Earth 108. https://doi.org/10.1029/2002JB002057.

Stich, D., Martínez-Solares, J.M., Custódio, S., Batlló, J., Martín, R., Teves-Costa, P., Morales, J., 2020. Seismicity of the Iberian Peninsula. In: Quesada, C., Oliveira, J. (Eds.), The Geology of Iberia: A Geodynamic Approach. Regional Geology Reviews. Springer, Cham. https://doi.org/10.1007/978-3-030-10931-8_3.

Stich, D., Morales, J., Ángel López-Comino, J., Araque-Pérez, C., Azañón, J.M., Ángel Dengra, M., Ruiz, M., Weber, M., 2024. Seismogenic structures and active creep in the Granada basin (S-Spain). Tectonophysics 882, 230368. https://doi.org/10.1016/j.tecto.2024.230368.

Thom, C., Kirkpatrick, J., 2023. A mechanism for transient creep in crustal shear zones. Geology. https://doi.org/10.1130/g50867.1.

Torii, K., Matsuoka, T., Onishi, K., Shiraishi, K., Aizawa, T., Yamanaka, Y., Ito, S., Kimura, T., Asano, Y., Takeda, T., 2008. Application seismic interferometry to natural earthquakes measured by small-scale array. In: San Antonio 2007 Annual Meeting, pp. 1362–1366. https://doi.org/10.1190/1.2792753.

Vasconcelos, I., Snieder, R., 2008. Interferometry by deconvolution: part 1 — Theory for acoustic waves and numerical examples. In: Seismic Interferometry: history and present Status. Society of Exploration Geophysicists. https://doi.org/10.1190/1.9781560801924. URL: doi:10.1190/1.9781560801924.

Ventisette, C., Montanari, D., Sani, F., Bonini, M., 2006. Basin inversion and fault reactivation in laboratory experiments. J. Struct. Geol. 28, 2067–2083. https://doi.org/10.1016/J.JSG.2006.07.012.

Viseras, C., Calvache, M., Soria, J., Fernández, J., 2003. Differential features of alluvial fans controlled by tectonic or eustatic accommodation space. Examples from the Betic cordillera, Spain. Geomorphology 50, 181–202. https://doi.org/10.1016/S0169-555X(02)00214-3.

Waldhauser, F., Michele, M., Chiaraluce, L., Di Stefano, R., Schaff, D.P., 2021. Fault planes, fault zone structure and detachment fragmentation resolved with high-precision aftershock locations of the 2016–2017 Central Italy sequence. Geophys. Res. Lett. 48, e2021GL092918. https://doi.org/10.1029/2021GL092918.

Wapenaar, K., 2003. Synthesis of an inhomogeneous medium from its acoustic transmission response. Geophysics 68 (5), 1756–1759. https://doi.org/10.1190/1.1620649.

Wapenaar, K., 2004. Retrieving the elastdynamic Green's function of an arbitrary inhomogeneous medium by cross correlation. Phys. Rev. Lett. 93, 1–4. https://doi.org/10.1103/PhysRevLett.93.254301.

Wapenaar, K., Fokkema, J., 2006. Green's function representations for seismic interferometry. Geophysics 71 (4), SI33–SI46. https://doi.org/10.1190/1.2213955.

Wapenaar, K., Slob, E., Snieder, R., 2008. Unified Green's function retrieval by cross correlation. In: Seismic Interferometry: history and present Status. Society of Exploration Geophysicists. https://doi.org/10.1190/1.9781560801924.

Wapenaar, K., Slob, E., Snieder, R., Curtis, A., 2010. Tutorial on seismic interferometry: part 2—underlying theory and new advances. Geophysics 75, 75A211–75A227. https://doi.org/10.1190/1.3463440.

Wortel, M.J., Spakman, W., 2000. Subduction and slab detachment in the Mediterranean-Carpathian region. Science 290 (5498), 1910–1917. https://doi.org/10.1126/science.290.5498.1910.

Wortel, M.J.R., Spakman, W., et al., 1992. Structure and dynamics of subducted lithosphere in the Mediterranean region. In: Proceedings of the Koninklijke Nederlandse Akademie van Wetenschappen, 95, pp. 325–347. https://research-portal.uu.nl/files/26677844/1992KNAW_Wortel_Spakman.pdf.

Yilmaz, O., 2001. Seismic Data Analysis: Processing, Inversion, and Interpretation of Seismic Data. volume 10. https://doi.org/10.1190/1.9781560801580.

Zhu, L., Kanamori, H., 2000. Moho depth variation in southern California from teleseismic receiver functions. J. Geophys. Res. Solid Earth 105 (B2), 2969–2980. https://doi.org/10.1029/1999JB900322.